



ARL-TR-7974 • APR 2017



Frequency-Domain Characterization of Optic Flow and Vision-Based Ocellar Sensing for Rotational Motion

**by Nil Z Gurel, Joseph K Conroy, Timothy Horiuchi, and
J Sean Humbert**

NOTICES

Disclaimers

The findings in this report are not to be construed as an official Department of the Army position unless so designated by other authorized documents.

Citation of manufacturer's or trade names does not constitute an official endorsement or approval of the use thereof.

Destroy this report when it is no longer needed. Do not return it to the originator.



Frequency-Domain Characterization of Optic Flow and Vision-Based Ocellar Sensing for Rotational Motion

by Nil Z Gurel

Graduate Student, University of Maryland

Joseph K Conroy

Sensors and Electron Devices Directorate, ARL

Timothy Horiuchi

Associate Professor, University of Maryland

J Sean Humbert

Associate Professor, University of Colorado–Boulder

REPORT DOCUMENTATION PAGE				Form Approved OMB No. 0704-0188	
<p>Public reporting burden for this collection of information is estimated to average 1 hour per response, including the time for reviewing instructions, searching existing data sources, gathering and maintaining the data needed, and completing and reviewing the collection information. Send comments regarding this burden estimate or any other aspect of this collection of information, including suggestions for reducing the burden, to Department of Defense, Washington Headquarters Services, Directorate for Information Operations and Reports (0704-0188), 1215 Jefferson Davis Highway, Suite 1204, Arlington, VA 22202-4302. Respondents should be aware that notwithstanding any other provision of law, no person shall be subject to any penalty for failing to comply with a collection of information if it does not display a currently valid OMB control number.</p> <p>PLEASE DO NOT RETURN YOUR FORM TO THE ABOVE ADDRESS.</p>					
1. REPORT DATE (DD-MM-YYYY) April 2017	2. REPORT TYPE Technical Report	3. DATES COVERED (From – To) 4/1/2016-8/1/2016 04/2016–07/2016			
4. TITLE AND SUBTITLE Frequency-Domain Characterization of Optic Flow and Vision-Based Ocellar Sensing for Rotational Motion				5a. CONTRACT NUMBER	
				5b. GRANT NUMBER	
				5c. PROGRAM ELEMENT NUMBER	
6. AUTHOR(S) Nil Z Gurel, Joseph K Conroy, Timothy Horiuchi, and J Sean Humbert				5d. PROJECT NUMBER	
				5e. TASK NUMBER	
				5f. WORK UNIT NUMBER	
7. PERFORMING ORGANIZATION NAME(S) AND ADDRESS(ES) US Army Research Laboratory ATTN: RDRL-SER-L 2800 Powder Mill Rd Adelphi MD 20783-1132				8. PERFORMING ORGANIZATION REPORT NUMBER ARL-TR-7974	
9. SPONSORING/MONITORING AGENCY NAME(S) AND ADDRESS(ES)				10. SPONSOR/MONITOR'S ACRONYM(S)	
				11. SPONSOR/MONITOR'S REPORT NUMBER(S)	
12. DISTRIBUTION/AVAILABILITY STATEMENT Approved for public release; distribution is unlimited.					
13. SUPPLEMENTARY NOTES					
14. ABSTRACT The structure of an animal's eye is determined by the tasks it must perform. While vertebrates rely on their 2 eyes for all visual functions, insects have evolved a wide range of specialized visual organs to support behaviors such as prey capture, predator evasion, mate pursuit, flight stabilization, and navigation. Compound eyes and ocelli constitute the vision-forming and sensing mechanisms of some flying insects. They provide signals useful for flight stabilization and navigation. In contrast to the well-studied compound eye, the ocelli, seen as the second visual system, sense fast luminance changes and allow for fast visual processing. Using a luminance-based sensor that mimics the insect ocelli and a camera-based motion-detection system, frequency-domain characterization of an ocellar sensor and optic flow (due to rotational motion) is analyzed. Inspired by the insect neurons that make use of signals from both vision-sensing mechanisms, complementary properties of ocellar and optic flow estimates are discussed.					
15. SUBJECT TERMS Bio-inspired sensing, rotational motion sensing, vision-based sensing, micro air vehicles, unmanned aerial vehicles, ocelli					
16. SECURITY CLASSIFICATION OF: Unclassified			17. LIMITATION OF ABSTRACT UU	18. NUMBER OF PAGES 72	19a. NAME OF RESPONSIBLE PERSON Joseph Conroy
a. REPORT Unclassified	b. ABSTRACT Unclassified	c. THIS PAGE Unclassified	19b. TELEPHONE NUMBER (Include area code) 301-394-2333		

Contents

List of Figures	v
List of Tables	viii
1. Introduction	1
1.1 Motivation	1
1.2 Contributions	2
2. Background	2
2.1 Structure and Function of Compound Eye	2
2.2 Structure and Function of Ocelli	4
2.3 Prior Works Inspired by Insect Ocelli	5
3. Frequency-Domain Characterization of Ocellar Sensor and Optic Flow	6
3.1 Introduction	6
3.2 Ocellar Sensor	7
3.3 Mathematical Model for the Ocellar Sensor	12
3.4 Optic Flow Computation	15
3.5 Experimental Setup	18
3.6 Magnitude-Squared Coherence	24
3.7 Ground Truth	25
3.8 Understanding Ocellar Sensor's "Valid Range"	26
3.9 Ocellar Sensor Frequency Characterization	29
3.9.1 Circuit Frequency Characterization	29
3.9.2 Sensor vs. Ground Truth Frequency Characterization	33
3.10 Ocellar Sensor–Gyro Voltage-Velocity Mapping	35
3.11 Performance-Related Parameters	36
3.11.1 Frame Rate	36
3.11.2 Window Size	38
3.11.3 Feature Points	40

3.11.4	Luminance Intensity	41
3.11.5	Photodiode Bending	42
3.12	Test Setup Limitations	43
4.	Sensor Fusion	44
4.1	Biological Background for Sensor Fusion	44
4.2	Fusion Approaches	45
4.3	Previous Sensor Fusion Implementations	46
4.4	Ocellar Sensor-Optic Flow Fusion Approach	47
5.	Conclusion and Future Work	52
5.1	Conclusion	52
5.2	Future Work	53
6.	References	55
List of Symbols, Abbreviations, and Acronyms		61
Distribution List		62

List of Figures

Fig. 1	Insect compound eye and ocelli (image used with Wikimedia Commons permissions: https://commons.wikimedia.org/wiki/File:Polistes_ocelli.jpg)	2
Fig. 2	Structure of compound eye (image used with Wikimedia Commons permissions: https://commons.wikimedia.org/wiki/File:Insect_compound_eye_diagram.svg).....	3
Fig. 3	Structure of ommatidium (image used with permission from Cronodon.com: http://cronodon.com/Copyright.html)	3
Fig. 4	Ocellus cross section (image used with Wikimedia Commons permissions: https://commons.wikimedia.org/wiki/File:Insect_ocellus_diagram.svg ; see Ref. 16)	4
Fig. 5	Circuit schematics of the 3-stage ocellar sensor. TSL14S photodiode outputs are band-pass filtered and antagonistically subtracted. Pitch rate (front–back) is inverted for sign change.	8
Fig. 6	Band-pass filter, with high-pass cutoff at 17 Hz and low-pass cutoff at 145 Hz.....	9
Fig. 7	Subtractor and inverter: Subtractor is used for antagonistic subtraction of filtered signals. Inverter is used for sign change for pitch rate. For equal resistors in both blocks, direct subtraction and direct inversion is satisfied.	10
Fig. 8	Simulated circuit in TI TINA simulation software	11
Fig. 9	Band-pass filter simulation results: 13.78 Hz high-pass cutoff and 174 Hz low-pass cutoff is observed. Phase starts at -90° at 1 mHz and reaches to -270° at 100 kHz.	11
Fig. 10	Mathematical model and assumptions: Photodiode in rotational motion sees the arbitrary luminance pattern as its azimuthal angle varies	12
Fig. 11	Optic flow vector for a pixel between 2 consecutive frames.....	16
Fig. 12	Optic flow during rotational and translational motion: without translational component (V), optic flow is an estimate of only angular velocity (ω)	19
Fig. 13	Illustration of test setup: Light source has its own DC supply to avoid issues of flickering; information from camera, microcontroller unit (MCU), gyro, and analog-to-digital converter (ADC) are transferred to the host computer via a USB hub.	19
Fig. 14	Camera scene (376×240 pixel image): DC light source is not in the FOV of the camera, which is moving along the x-direction.....	20

Fig. 15	Overall test setup: Ocellar sensor is positioned in front of light source. Motor is giving rotational motion to the setup along its shaft axis. The motor shaft is in vertical orientation, moving the components on it ..21
Fig. 16	Test setup components: Camera sees the scene shown in Fig. 17. Camera on the right is not used due to performance issues.....21
Fig. 17	System block diagram: All of the data collected are stored in laptop .22
Fig. 18	Serial message structure from ocelli to microcontroller includes 2 header, ocelli data, and gyro data bytes22
Fig. 19	Post-processing block diagram: Optic flow vectors are computed and extracted as a text file. The bag file is parsed, interpolated, and processed for data analysis.....24
Fig. 20	Motor velocity and gyro frequency response, as seen by Vicon motion-detection system as input: Frequencies after 10 Hz were shown to prove the decrease in coherence out of controlled motion frequencies. Gyroscope shows a flatter magnitude response and higher coherence than motor velocity; therefore, it was chosen to be the ground truth. .26
Fig. 21	Unbent photodiode output vs. motor shaft azimuthal position: Photodiode outputs increase as they pass by the light source. FOVs are not overlapping.27
Fig. 22	Bent photodiode output vs. motor shaft azimuthal position: Photodiode FOVs are partially overlapping, which is required for the ocellar sensor to work. In this (incorrect) configuration, there are angles where simulated roll motions do not produce any change in the photodiode outputs.....27
Fig. 23	Ocelli in valid range: (above) symmetric photodiode raw output; (below) gyro and ocelli output for motor azimuthal position (-0.2 to 0.2 radians). Ocelli output is in agreement with gyro in this range....28
Fig. 24	Ocelli in invalid range: (above) asymmetric photodiode raw output; (below) gyro and ocelli output for motor azimuthal position (-1.2 to 0.2 radians). Ocelli output is not in agreement with gyro in this range.....29
Fig. 25	Band-pass filter simulated AC transfer characteristic at 0.1–10 Hz: Magnitude increases with 20 dB/decade. Phase drops from -90° to -125° at the end of 10 Hz.30
Fig. 26	Right and left band-pass filter measured AC transfer characteristics at 0.1–10 Hz: Magnitude and phase plots are in agreement with simulation (Fig. 28).....30
Fig. 27	LED sweeping: LED was taped to photodiode and power-supply signal is swept between 3 and 150 Hz.31
Fig. 28	Right and left band-pass filter simulated transfer characteristics between 1 and 100 Hz; simulation is shown to compare with LED sweeping results in Fig. 32.....32

Fig. 29	Right band-pass filter measured transfer characteristics in response to LED chirp between 3 and 100 Hz: magnitude increases 20 dB/decade and phase drops from -105° to -180° (in agreement with simulation in Fig. 31).....	32
Fig. 30	Ocelli frequency response with respect to gyro as input: Frequencies after 10 Hz were shown to prove the decrease in coherence out of controlled motion frequencies. Ocellar magnitude is relatively flat, showing around 1dB difference from beginning to end. Phase delay reaches to -15° at 10 Hz.	33
Fig. 31	Time signals of gyro, ocelli, and optic flow in 0.5-, 1-, 5-, and 10-Hz windows; all sensor outputs are scaled to match gyro (rad/s) at each window.....	34
Fig. 32	Frequency response of optic flow with respect to gyro as input: Overall magnitude decrease is 1.42 dB. Phase delay reaches to -35° at 10 Hz.....	35
Fig. 33	Ocelli-gyro mapping plot shows the expected ocelli output (V) for a given gyro measurement (rad/s). Ocelli output is monotonically increasing with increasing gyro values.	36
Fig. 34	Optic flow frequency response with different frame rates, as seen by input gyro: As the frame rate decreases, roll-off at higher frequencies is steeper. Higher frame rate results in better coherence. Phase delay does not change due to frame rate.....	37
Fig. 35	Optic flow frequency response with different window sizes ($w = 10, 20, 30, 40$), as seen by input gyro: Very small windows (10×10 pixel) result in erroneous magnitude response. Magnitude response and coherence improve as window size increases, phase delay remains the same.	39
Fig. 36	Optic flow frequency response with different window sizes ($w = 50, 60, 70$), as seen by input gyro: After 50×50 -pixel window, magnitude, phase, and coherence plots do not change.	39
Fig. 37	Camera scene (10×10 feature points)	40
Fig. 38	Camera scene (4×4 feature points)	40
Fig. 39	Optic flow frequency response with different number of feature points (f), as seen by input gyro: 2×2 feature points result in erroneous magnitude plot. As the feature points increase, magnitude and phase plots do not show much change; however, coherence improves.	41
Fig. 40	Light source input power vs. ocelli peak-to-peak amplitude: Luminance increase linearly increases the peak-to-peak amplitude. DC light source is specified in Table 3.	42
Fig. 41	Bending illustration: The photodiodes should share an intersecting FOV toward the light source for the sensor to operate. Bending values $30^\circ < \beta < 45^\circ$ were observed to give symmetric photodiode outputs. $B = 90^\circ$ completely overlaps the FOVs, without distinct horizons for each photodiode.	43

Fig. 42	Illustration of complementary filter	45
Fig. 43	Frequency response ocelli, optic flow, and their complementary fusion: Fourth-order Butterworth filter was used to high-pass ocelli and low-pass optic flow. The normalized cutoff frequency had to be kept very small to make use of ocelli's relatively flat magnitude and less-delayed phase. Fused response shows coherence is better than optic flows.....	48
Fig. 44	Frequency response ocelli, optic flow, and their weighted-average fusion: Ocelli and optic flow time-domain signals are combined to obtain a result close to ocelli.....	49
Fig. 45	Magnitude response of ocelli with different luminance values and optic flow at 30 fps: Increasing luminance implies higher magnitude for ocelli ($L_1 < L_2 < L_3 < L_4 < L_5$). Ambient luminance change brings adaptive gain necessity. Upper figure is the magnitude-scaled versions of ocelli response, not derived from real luminance values.....	50
Fig. 46	Hypothetical sensor decision approach: Adjust ocelli gain by continuously computing error between gyro/OF and ocelli; check if ocelli is valid to use by comparing gyro/OF; use ocelli if comparisons allow.....	51
Fig. 47	Hypothetical ocelli gain adjustment approach: Gains > 1 are tuned by noninverting op-amp. Gains < 1 are tuned by voltage divider. The tuned outputs are compared with lookup table and microcontrollers iteratively tune the digital potentiometers until error threshold is low enough.....	52

List of Tables

Table 1	Circuit components	9
Table 2	Band-pass filter characteristics	10
Table 3	Experiment components.....	20

1. Introduction

1.1 Motivation

The design of sensing mechanisms for small unmanned aircraft systems (sUAS) has many tradeoffs due to limited budgets for power consumption, size, weight, and the need for both speed and accuracy in a wide range of operating conditions. Traditionally, inertial measurement units (gyroscopes and accelerometers) are used to obtain velocity and position data. There has been a rapid evolution of these sensor systems in recent years toward integrated accelerometer and gyroscope packages that include both digitization and signal conditioning (e.g., filtering). As the vehicle sizes have continued to decrease, faster sensing is needed due to the increased susceptibility of the aircraft to tiniest of disturbances.

Looking to nature, several species of flying insects have been demonstrated to possess exceptional stability and acrobatic capabilities that match the types of missions that engineers are trying to accomplish. They provide examples of robust stability given similar limitations of sensing and processing. The insect body is a multimodal sensor network. Information from visual, proprioceptive, tactile, and inertial receptors is collected to provide information about the state of the insect with respect to its environment.¹ Instead of the digital architecture used in traditional sUAS, insects have analog connections between their sensory systems and their flight motor neurons. Analog architecture makes them capable of closing feedback loops at high speeds, becoming very useful for fast stabilization for sudden disturbances. Bio-inspired sensing techniques based on these species present an attractive way for microaerial-vehicle sensor design.

Many flying insects employ 2 visual systems, the compound eyes and the ocelli (simple eyes). From the behavioral and electrophysiological experiments cited in the next sections, the compound eyes and ocelli are thought to work together. Overall, compound eyes are sensitive to a wide range of information, such as proximity to obstacles, relative velocity, and rotation rate.²⁻⁴ These tasks increase the information-processing time for the compound eyes, making them unable to provide fast responses for sudden disturbances. Insects have to balance themselves quickly to survive. Ocelli, responsible for a fewer number of tasks compared to compound eyes, have less processing time,^{5,6} which makes them favorable to detect sudden disturbances. Inspired by the complementary nature of ocelli and compound eyes, this report attempts to characterize the frequency response of an ocellar sensor and optic flow, and ultimately proposes the fusion of 2 sensors for low-cost, wide-field, visual rotational motion sensing.

1.2 Contributions

The contributions of this report are listed as follows:

- The comparative open-loop frequency characterization of optic flow and a luminance-dependent analog rotation-rate sensor that is thought to mimic insect ocelli was conducted.
- Sensitivity analysis was done to analyze the parameters that affect the optic flow and ocellar sensor performance in rotational motion.

2. Background

2.1 Structure and Function of Compound Eye

The compound eyes and ocelli are shown in Fig. 1, head of a flying insect (Polistes). The structure of compound eyes (large, 2 on the sides) is seen in Fig. 2. The compound eyes are composed of units called ommatidia. Each ommatidium unit functions as a separate visual receptor, consisting of a lens, cornea, a crystalline cone, light-sensitive visual cells, and pigment cells (Fig. 3). There may be up to 30,000 ommatidia in a single compound eye. The image perceived is a combination of inputs from ommatidia pointing at slightly different directions (as seen in Fig. 2, ommatidia units make up a conic surface). A mosaic-like vision of the environment is rendered.^{2,3}

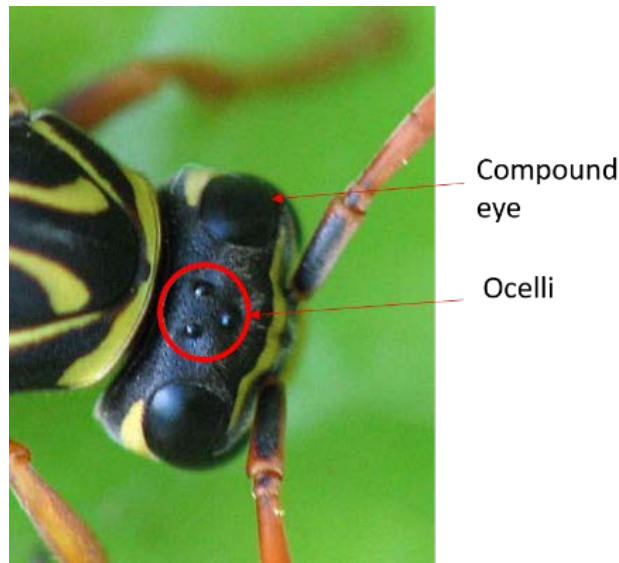


Fig. 1 Insect compound eye and ocelli (image used with Wikimedia Commons permissions: https://commons.wikimedia.org/wiki/File:Polistes_ocelli.jpg)

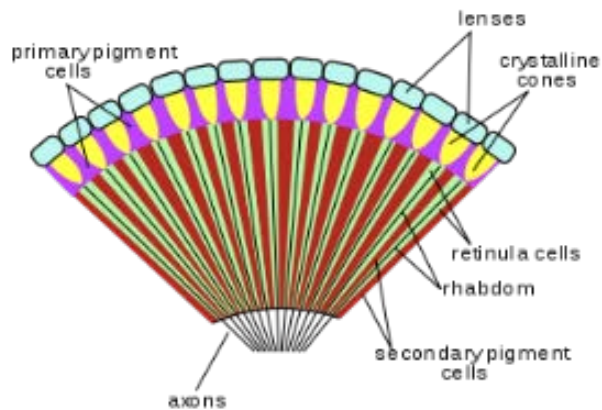


Fig. 2 Structure of compound eye (image used with Wikimedia Commons permissions: https://commons.wikimedia.org/wiki/File:Insect_compound_eye_diagram.svg)

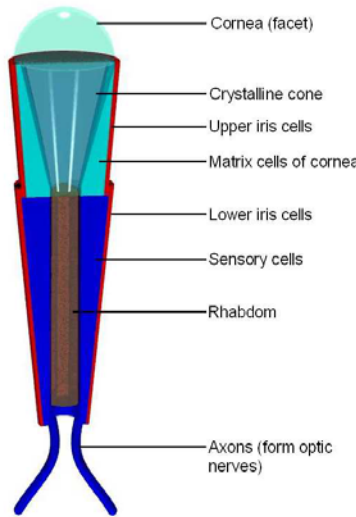


Fig. 3 Structure of ommatidium (image used with permission from Cronodon.com: <http://cronodon.com/Copyright.html>)

Vision process starts at ommatidia. Ommatidia photoreceptors capture patterns of luminance from the visual environment. The captured signal is conditioned through lamina plate. The output of lamina is thought to be the input to medulla.^{7,8} The medulla outputs optic flow-like patterns to lobula, and lobula processes these outputs.^{9–13} The output signals of lamina neurons are segregated into different pathways, performing functions such as color discrimination, motion detection, and intensity encoding. Neurons responding to motion are found in lobula. They are thought to receive inputs from hypothetical neural elements called Reichardt Detectors, or elementary motion detectors (EMDs), residing in medulla and calculating motion from the pixel-based information with a mechanism called

Reichardt correlation.¹⁴ This hypothetical mechanism is proposed to understand how a neuron, which is only receiving luminance input, is able to compute motion. Frye.¹⁵ depicts the key components of this algorithm, which are 2 inputs (red, as photoreceptors), a time delay on one input (d), and multiplication on correlated signals.

- 1) Photons from a visual scene move from left to right.
- 2) Photons activate the first receptor.
- 3) The signal from the first receptor is delayed with d as the photons move to the second receptor.
- 4) Photons activate the second photoreceptor. Both the delayed signal (from first receptor) and the undelayed signal (from second receptor) converge simultaneously onto a multiplication stage, producing a signal related to direction of motion. Conversely, photons passing from right to left will output zero for the opposite direction, since there is no delay component that will deliver simultaneous inputs to multiplication stage.

2.2 Structure and Function of Ocelli

Ocelli differ from the compound eye in that they have only a single lens covering an array of photoreceptors, as seen in Fig. 4. Ocelli are found in the frontal surface of the head of many insects. Ocelli tend to be larger in flying insects (bees, dragonflies, locusts) and are typically found as a triplet. Two lateral ocelli are found in the left and right of the head, while a median ocellus is directed frontally.

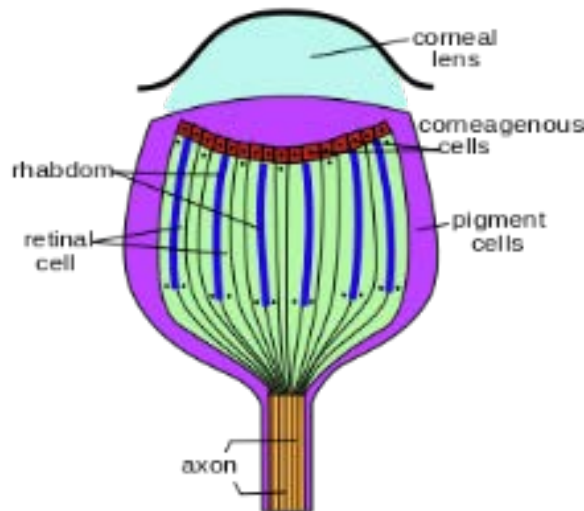


Fig. 4 Ocellus cross section (image used with Wikimedia Commons permissions: https://commons.wikimedia.org/wiki/File:Insect_ocellus_diagram.svg; see Ref. 16)

Various studies have been conducted to reveal the function of ocelli for different insects. Although it is called an “eye”, ocellus is claimed to be underfocusing the image, hence showing hardly any image details for a locust. In contrast to the “underfocusing” information for the locust,¹⁷ suggests that the dragonfly ocellus, which is believed to be highly evolved, is able to detect some image details.

It is also suggested that the temporal and spatial filtering characteristics of locust ocelli neurons are well suited to detect instability in flight.^{18,19} The stabilization in flight studies were summarized by Heisenberg and Reinhard,⁴ most of which studies are conducted by releasing dragonflies with ablated ocelli. Dragonflies show unstable flight attitudes without ocelli. Kastberger and Schumann²⁰ evaluate the flight behavior of bees with and without occluded ocelli, stating that normal bees (without occlusion) show quicker flight behaviors.

Another characteristic of ocelli is higher photic sensitivity, compared to the compound eye for locusts¹⁸ and bees.²¹ This information is useful if we think of the ocelli as integrators of the overall intensity or a blurred visual field. If the photic sensitivity is high, small changes in light intensity will be sensed. Taking into account that the images sensed by the ocelli are highly blurred, ocelli should be concerned with the overall image intensity. Studies of dragonflies^{22,23} and locusts²⁴ claim that ocelli are rotation detectors, important for gaze stabilization. Research by Schuppe and Hengstenberg²⁵ also shows gaze stabilization cues by the ocelli. The beginning and end of daily activities of insects depend on light intensity. Studies of bees,²³ crickets,²⁶ and moths^{27–29} claim that the ocelli perceive low light intensity to control daily activities.

Compared to ocelli, compound eyes offer a panoramic field of view (FOV) and high temporal resolution, with optic flow computation abilities.^{30–32} These features are beneficial for tasks like visually guided navigation (e.g., obstacle avoidance, landing strategy, saccade response, hovering strategy clutter response, collision response, and fixation strategy) each of which is described by Barrows et al.³³ with specific test setups for bees and drosophilae.

2.3 Prior Works Inspired by Insect Ocelli

Because of the prominent computation advantages, simplicity, and applicability to small-scale world, ocelli-inspired vision sensors have been developed by many groups. These implementations mainly focus on closed-loop attitude control, outputting pitch, and roll angle. Neumann and Bülthoff³⁴ present a simulation model of an autonomous agent flying through a virtual environment with a daylight sky model. It uses over 200 receptors to detect local intensities. These receptors are distributed evenly between adjacent directions on an agent body coordinate system.

The average intensity difference between 2 directions is computed to estimate the roll angle. Subsequently, a simulation of an eye model with a special receptor distribution was presented in a virtual environment in their 2002 report.³⁵ The ocelli-like “wide-field measurement units” that use a locally weighted intensity as receptor response are subtracted in adjacent directions. Using an EMD and ocelli outputs, optimal receptive fields for attitude estimation, yaw rotations and nearness are derived. A 2003 study³⁶ implements ocelli, haltere (an organ responsible for balance in flying insects), optic flow, and magnetic flow sensors for a micromechanical flying insect. These sensors were used to estimate body attitude relative to a fixed frame, body rotational velocities, obstacle avoidance, and heading adjustment, respectively. The ocelli consist of 4 photodiodes, arranged in a pyramidal configuration. The 2 output signals are obtained by subtracting the opposite photodiode outputs. Schenato et al.³⁷ use this implementation and proposes a stabilizing attitude control law for a sinusoidal intensity function. Javaan et al.³⁸ demonstrate an embedded implementation of ocelli-like sensor. It uses the difference between ultraviolet and green photodiode signals to obtain attitude estimation, stating that this reduces the biasing effect of clouds and the sun. Kerhuel et al.³⁹ use a camera to track a reference heading point and perform gaze stabilization by using the difference between reference and instantaneous heading signal. Moore et al.⁴⁰ use camera images that are classified by the intensity information in the YUV (luminance, blue, red) channel into sky and ground regions to estimate roll and pitch angles. Javaan and Akiko⁴¹ use 4 ultraviolet/green photodiode pairs to detect attitude angle and demonstrates roll attitude tracking on an aircraft. A 2014 study⁴² proposes an ocelli-based sensor, which is also used in this work, to output roll and pitch rate, rather than angle. This sensor was used for the frequency characterization in Section 3 of this report.

3. Frequency-Domain Characterization of Ocellar Sensor and Optic Flow

3.1 Introduction

Gremillion et al.⁴² present experimental data that use the complementary response of an analog ocellar sensor and a commercial optic flow sensor. Inspired by this complementary response information and cues from insect ocelli and compound eye complementary task mechanism, we designed a test platform that generates rotational motion to characterize the frequency-domain response of both optic flow and an ocellar sensor, and gathers information from different sources such as motor controller, microcontroller, and gyroscope. The optic flow is computed using the images collected by a camera and fisheye lens. A microelectromechanical systems

gyroscope and a Vicon motion-detection system are used as ground truth. This section discusses the ocelli and optic flow frequency response characteristics and the performance parameters for the ocelli and optic flow computation.

3.2 Ocellar Sensor

The ocellar sensor (based on work by Gremillion et al.⁴²) gives roll and pitch rate estimates using the luminance change sensed by right-left or front-back photodiode pairs. The luminance signals from left and right photodiodes are band-pass filtered. The high-pass filter portion serves as the differentiator element to estimate rate information introduced by luminance change. The high-frequency cutoff was added to reject the flickering noise for indoor usage. The filtered signals from the photodiodes are antagonistically subtracted from each other (left-right or front-back) to obtain roll and pitch rate estimates. The overall circuit schematics are shown in Fig. 5 and the circuit components are listed in Table 1.

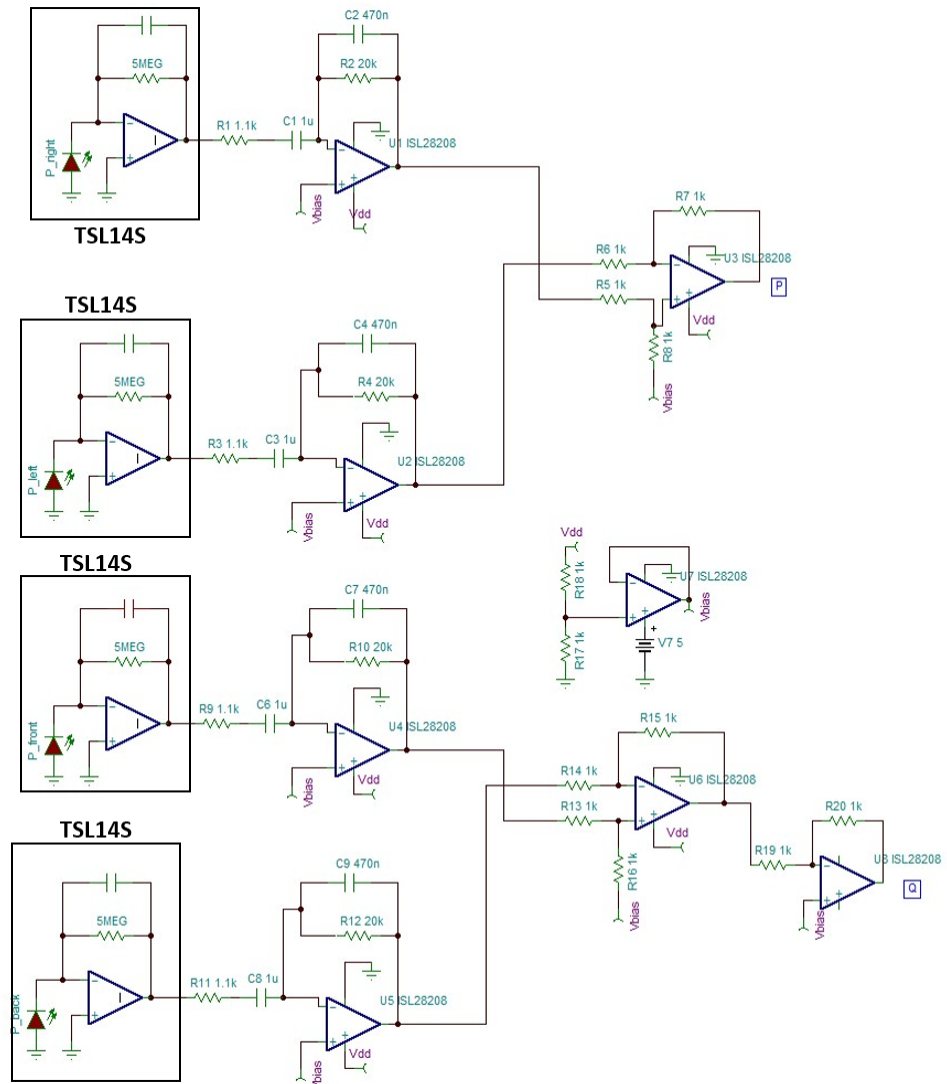


Fig. 5 Circuit schematics of the 3-stage ocellar sensor. TSL14S photodiode outputs are band-pass filtered and antagonistically subtracted. Pitch rate (front–back) is inverted for sign change.

Table 1 Circuit components

Component	Value/part number
R1,3,9,11	1.1 kΩ
R5,6,7,8,13,14,15,16,17,18,19,20	1 kΩ
R2,4,10,12	20 kΩ
C1,3,6,8	1 μF
C2,4,7,9	470 nF
Operational amplifier	ISL28208
photodiode	TSL14S
Vdd	5 V

The circuit consists of 3 stages:

1) *Light-to-Voltage Conversion*

Light-to-voltage conversion by a TSL14S optical sensor⁴³ that combines a photodiode and a transimpedance amplifier. The sensor has a wideband spectral response characteristics between 320 and 1050 nm. Its peak output is at 640 nm. The output voltage from this element is the electrical equivalent of luminance seen by the photodiode.

2) *Band-Pass Filtering*

This stage consists of an active bandpass filter with a designed high-pass cutoff at 17 Hz and low-pass cutoff at 145 Hz (see Fig. 6).

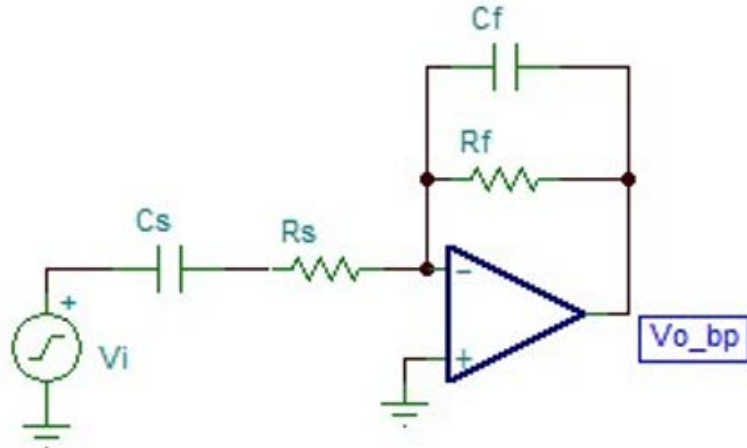


Fig. 6 Band-pass filter, with high-pass cutoff at 17 Hz and low-pass cutoff at 145 Hz

The input–output relationship of a high-pass filter is modeled as

$$V_o(t) = -R_f C_s \frac{d}{dt} (V_i(t)) \quad . \quad (1)$$

The input voltage is the luminance value from the TSL14S package. The output voltage approximates the luminance time rate of change. The function of the low-pass filter is to attenuate high-frequency noise. The final band-pass filter transfer function is in Eq. 2.

$$\left(\frac{V_o(s)}{V_i(s)}\right) = \frac{sC_S R_F}{s^2 C_F R_F C_S R_S + s(C_F R_F + C_S R_S) + 1} . \quad (2)$$

The characteristic quantities of this second order transfer function are the low-pass cutoff frequency ω_L , high-pass cutoff frequency ω_H , and maximum input–output gain A_{max} , specified in Table 2.

Table 2 Band-pass filter characteristics

$$\begin{aligned}\omega_L &= \frac{1}{R_F C_F} && 106 \text{ rad/s (16.9 Hz)} \\ \omega_H &= \frac{1}{R_S C_S} && 909 \text{ rad/s (145 Hz)} \\ A_{max} &= \frac{-R_F}{R_S} && -18.2\end{aligned}$$

3) Linear combination stage:

This stage includes a difference amplifier to subtract right–left filter outputs and front–back filter outputs. The difference amplifier output from the right–left inputs estimates the roll rate. The difference amplifier output from the front–back inputs is inverted (for sign change) by an inverting amplifier. Inverting amplifier output estimates the pitch rate (see the blocks in Fig. 7).

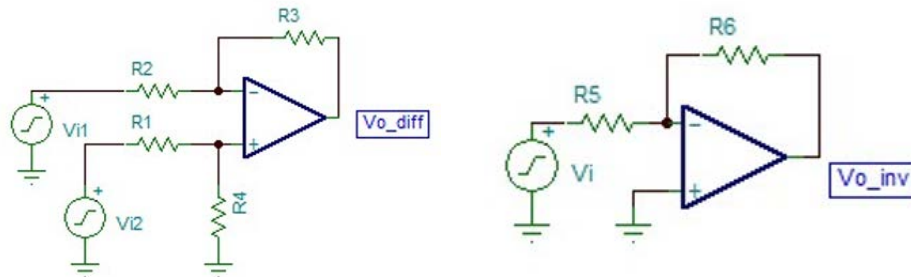


Fig. 7 Subtractor and inverter: Subtractor is used for antagonistic subtraction of filtered signals. Inverter is used for sign change for pitch rate. For equal resistors in both blocks, direct subtraction and direct inversion is satisfied.

For $R_{1,2,3,4,5,6} = 1k\Omega$, the outputs V_{o_diff} and V_{o_inv} are modeled as

$$V_{o_diff} = V_{i2} - V_{i1} \quad (3)$$

$$V_{o_inv} = -V_i . \quad (4)$$

The bandpass filter was simulated (Fig. 8) using the macro model of the ISL28208 operational amplifier in the Tina TI SPICE-based simulation program. The simulated circuit and alternating current (AC) transfer characteristics for frequencies between 1 mHz and 1 MHz are seen in Fig. 9. According to the simulation (due to the zero in the denominator of the transfer function) the amplitude is increased by 20 dB/decade until it hits the first pole. The high-pass -3 dB frequency is seen as 13 Hz. The maximum amplitude is 5.58 dB around 55 Hz. The low-pass -3 dB frequency is seen as 175 Hz.

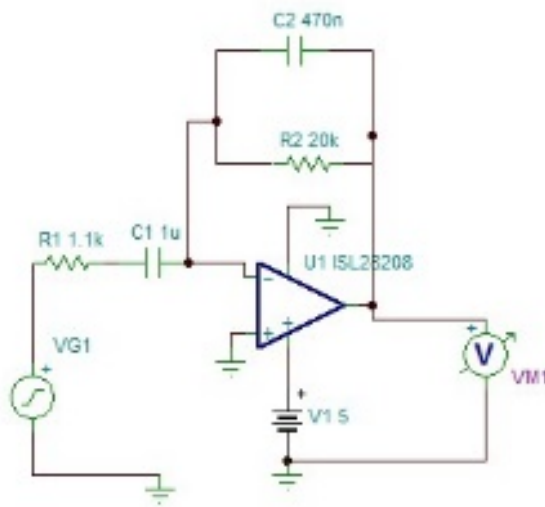


Fig. 8 Simulated circuit in TI TINA simulation software

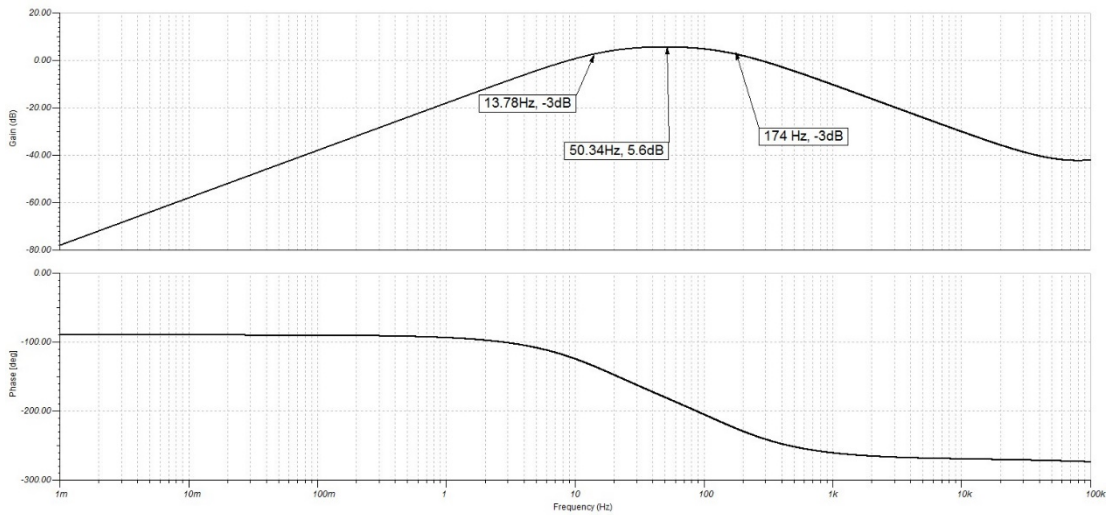


Fig. 9 Band-pass filter simulation results: 13.78 Hz high-pass cutoff and 174 Hz low-pass cutoff is observed. Phase starts at -90° at 1 mHz and reaches to -270° at 100 kHz.

3.3 Mathematical Model for the Ocellar Sensor

With reference to Fig. 10, the variables used to explain the ocellar sensor are as follows:

γ : Azimuth angle of the photodiode

φ : Angular position

\emptyset : Photodiode field of view

$\vartheta = \frac{d\gamma}{dt} = \dot{\gamma}$: Angular speed

$L(\gamma)$: Luminance, assume periodic

α : Light source field of luminance

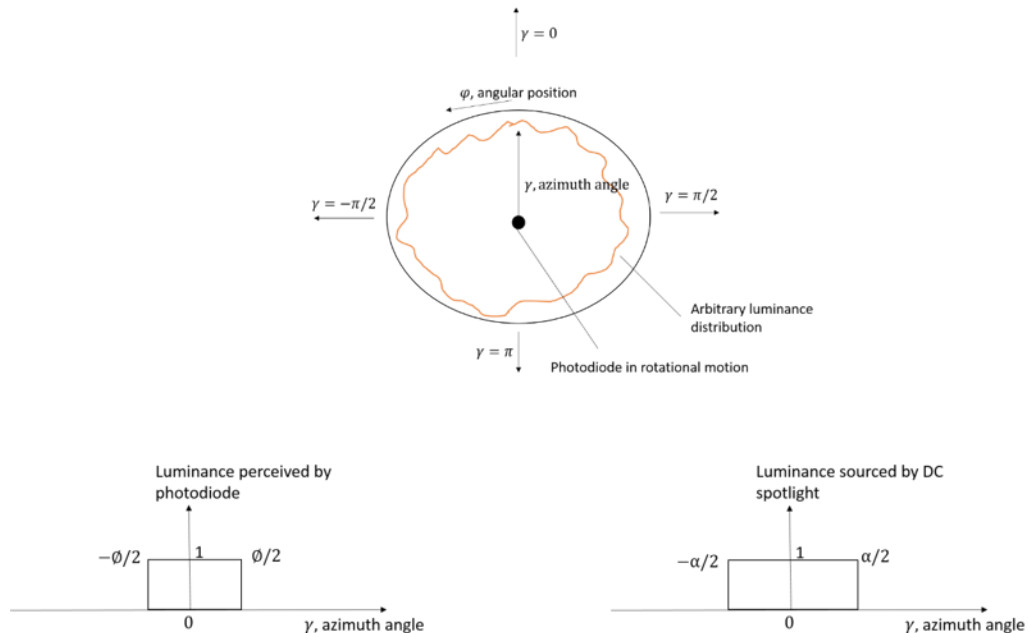


Fig. 10 Mathematical model and assumptions: Photodiode in rotational motion sees the arbitrary luminance pattern as its azimuthal angle varies

The test setup has a DC spotlight source, which acts as “the sun”. For simplicity, luminance is modeled as a rectangular function with fixed edges from $-\alpha/2$ to $\alpha/2$. Photodiode FOV is also modeled as a rectangular function with edges at FOV edges, $-\emptyset/2$ to $\emptyset/2$

$h(\emptyset, \gamma)$: Photodiode field of view function modeled as a rectangular filter with edges at $-\emptyset/2$ and $\emptyset/2$

p : Photodiode output (or signal input to bandpass filter)

$*$: convolution operation

The photodiode integrates the luminance in its FOV, as $h(\emptyset, \gamma)$

$$\rho = \int_{FOV} L(\gamma) d\gamma = L(\gamma) * h(\emptyset, \gamma) = L_h(\gamma) . \quad (5)$$

Let $L_h(\gamma)$ be a photodiode output taken at the azimuth angle γ . While the circuit is in rotational motion with angular speed ϑ , this photodiode output becomes $L_h(\gamma - \vartheta t)$ at time t . Thus, the photodiode output encodes both spatial (γ) and temporal (ϑt) information.

$$L_h(\gamma) \rightarrow L_h(\gamma - \vartheta t) . \quad (6)$$

Since the photodiode output is in 2 domains, the Fourier transform with respect to both spatial and temporal variables should be taken in order to express it in Fourier domain.

$L_h(\gamma, t)$: denotes the function in spatial and temporal domain

$\widehat{L}_h(f_\gamma, f_t)$: denotes the Fourier transform $L_h(\gamma, t)$

$$L_h(\gamma - \vartheta t) \xrightleftharpoons{FT_{\gamma,t}} \widehat{L}_h(f_\gamma, f_t) . \quad (7)$$

Properties used:

Shifting property in time/space and Fourier domain:

$$x(\gamma - \beta) \xrightleftharpoons{FT_\gamma} \widehat{x}(f_\gamma) e^{-j2\pi f_\gamma \beta} . \quad (8)$$

Convolution:

$$x(\gamma) * y(\gamma) \xrightleftharpoons{FT_\gamma} \widehat{x}(f_\gamma) \widehat{y}(f_\gamma) . \quad (9)$$

Taking the Fourier transform with respect to spatial variable γ :

$$L_h(\gamma - \vartheta t) \xrightleftharpoons{FT_\gamma} \widehat{L}_h(f_\gamma) e^{-j2\pi (\vartheta f_\gamma) t} . \quad (10)$$

Then, taking the Fourier transform with respect to temporal variable t gives the frequency domain of a rotational motion:

$$\widehat{L}_h(f_\gamma, f_t) = \widehat{L}_h(f_\gamma) \delta(f_t + \vartheta f_\gamma) \quad (11)$$

$$L_h(\gamma - \vartheta t) \xrightleftharpoons{FT_{\gamma,t}} \widehat{L}_h(f_\gamma) \delta(f_t + \vartheta f_\gamma) . \quad (12)$$

This means that all the energy of the rotating photodiode output is contained in a plane of the spatiotemporal frequencies domain.^{44,45} The equation of this plane is

$$f_t + \vartheta f_y = 0 \quad . \quad (13)$$

The rectangular luminance function can be described as $L_h(\gamma - \vartheta t) \sim rect(x, t)$ with space and time axis. A rectangular pulse in space $rect(x)$ has sinc form in frequency domain:

$$rect(x) \xleftrightarrow{FT_x} \frac{\sin(\pi f_x)}{\pi f_x} \quad . \quad (14)$$

The corresponding frequency spectrum appears as a cut of spatial spectrum⁴⁶ $\frac{\sin(\pi f_x)}{\pi f_x}$ by a wall of Dirac situated in the direction of $f_t + \vartheta f_y = 0$

Overall,

$$\widehat{L}_h(f_\gamma, f_t) = \widehat{L}_h(f_\gamma) \delta(f_t + \vartheta f_\gamma) \quad . \quad (15)$$

Equation 15 represents the photodiode output given as input to the bandpass filter in the circuit. Bandpass filtering is a temporal process; thus, the bandpass function has only temporal variable. Let the bandpass filter transfer function in time and Fourier domain be defined as

$$BPF(t) \xleftrightarrow{FT_t} \widehat{BPF}(f_t) \text{ or } \widehat{BPF}(s) \quad . \quad (16)$$

From the ocellar sensor section, $\widehat{BPF}(s)$ is defined as

$$\widehat{BPF}(s) = \frac{V_o(s)}{V_i(s)} = \frac{sC_sR_F}{s^2C_F R_F C_S R_S + s(C_F R_F + C_S R_S) + 1} \quad . \quad (17)$$

The output of the bandpass filter can be written as

$$L_{h,BPF}(\gamma, t) = L_h(\gamma - \vartheta t) * BPF(t) \quad . \quad (18)$$

The Fourier transform of the output becomes

$$L_{h,BPF}(\gamma, t) \xleftrightarrow{FT_{\gamma,t}} \widehat{L}_{h,BPF}(f_\gamma, f_t) \quad (19)$$

$$L_h(\gamma - \vartheta t) * BPF(t) \xleftrightarrow{FT_{\gamma,t}} \widehat{L}_h(f_\gamma) \delta(f_t + \vartheta f_\gamma) \widehat{BPF}(f_t) \quad . \quad (20)$$

This output represents the luminance output filtered by one photodiode. Assume another photodiode is has a different azimuth angle, $\gamma - \beta$, offset by β from the first photodiode. The luminance perceived by it will be

$$L_{h,\beta}(\gamma - \beta - \vartheta t) \xrightarrow{FT_{\gamma,t}} \widehat{L_{h,\beta}}(f_\gamma, f_t, \beta) \quad (21)$$

$$L_{h,\beta,BPF}(\gamma, t, \beta) \xrightarrow{FT_{\gamma,t}} \widehat{L_{h,\beta,BPF}}(f_\gamma, f_t, \beta) \quad (22)$$

$$\widehat{L_{h,\beta}}(f_\gamma, f_t, \beta) = \widehat{L_{h,\beta}}(f_\gamma) \delta(f_t + \vartheta f_\gamma) e^{-j2\pi f_\gamma \beta} \quad . \quad (23)$$

After bandpass filtering, the Fourier transform of the second output becomes

$$\widehat{L_{h,\beta,BPF}}(f_\gamma, f_t, \beta) = \widehat{L_{h,\beta}}(f_\gamma) \delta(f_t + \vartheta f_\gamma) e^{-j2\pi f_\gamma \beta} \widehat{BPF}(f_t) \quad . \quad (24)$$

The difference amplifier implements direct subtraction between 2 bandpass filter outputs as the roll rate estimation. Let the roll rate be denoted as $p(\gamma, t)$

$$p(\gamma, t) = L_{h,BPF}(\gamma, t) - L_{h,\beta,BPF}(\gamma, t) \quad (25)$$

$$p(\gamma, t) \xrightarrow{FT_{\gamma,t}} \widehat{P}(f_\gamma, f_t) \quad (26)$$

$$\begin{aligned} \widehat{P}(f_\gamma, f_t) &= \widehat{L_{h,BPF}}(f_\gamma, f_t) - \widehat{L_{h,\beta,BPF}}(f_\gamma, f_t, \beta) = \widehat{L_h}(f_\gamma) \delta(f_t + \vartheta f_\gamma) \widehat{BPF}(f_t) - \\ &\widehat{L_{h,\beta}}(f_\gamma) \delta(f_t + \vartheta f_\gamma) e^{-j2\pi f_\gamma \beta} \widehat{BPF}(f_t) = \widehat{BPF}(f_t) \delta(f_t + \vartheta f_\gamma) [\widehat{L_h}(f_\gamma) - \\ &\widehat{L_{h,\beta}}(f_\gamma) e^{-j2\pi f_\gamma \beta}] \end{aligned} \quad . \quad (27)$$

Thus, the circuit output depends on

- Photodiode FOV
- Bandpass filter characteristics
- Luminance function $L(\gamma)$
- Photodiode angular separation β

The photodiode field-of-view and bandpass filter characteristics are inherent in the circuit under test, and these variables are fixed. We have control of the luminance function $L(\gamma)$ and photodiode angular separation β . The luminance function is also dependent on the light intensity (or, the input power given to light source).

3.4 Optic Flow Computation

Optic flow is an approximation of apparent motion of brightness patterns observed when an observer (i.e., camera) is moving relative to the objects it images. Optic flow methods try to calculate where a pixel in Image A goes to in a consecutive Image B. In 2 dimensions, optic flow specifies how much a pixel of an image moves between adjacent series.⁴⁷ The basis of optic flow is the brightness constancy equation, which eventually forms the 2-D motion constraint.

Assume that $I(x,y,t)$ is the intensity of pixel positioned at location (x,y) in a frame taken at time t . In the frame taken at time $(t+\Delta t)$, this pixel moves to the location $(x+\Delta x, y+\Delta y)$ (see Fig. 11).

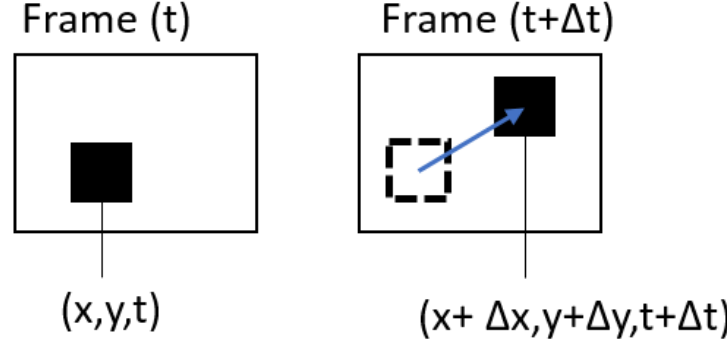


Fig. 11 Optic flow vector for a pixel between 2 consecutive frames

Assuming the brightness of the pixel does not change over time;

$$I(x, y, t) = I(x + \Delta x, y + \Delta y, t + \Delta t) \quad . \quad (28)$$

Performing first-order Taylor Series expansion about $I(x, y, t)$:

$$I(x + \Delta x, y + \Delta y, t + \Delta t) = I(x, y, t) + \frac{\partial I}{\partial x} \Delta x + \frac{\partial I}{\partial y} \Delta y + \frac{\partial I}{\partial t} \Delta t + \text{higher order terms} \quad . \quad (29)$$

Assuming very small motion and ignoring the higher-order terms,

$$\frac{\partial I}{\partial x} \Delta x + \frac{\partial I}{\partial y} \Delta y + \frac{\partial I}{\partial t} \Delta t = 0 \quad . \quad (30)$$

Dividing everything by Δt :

$$\frac{\partial I}{\partial x} \frac{\Delta x}{\Delta t} + \frac{\partial I}{\partial y} \frac{\Delta y}{\Delta t} + \frac{\partial I}{\partial t} \frac{\Delta t}{\Delta t} = 0 \quad . \quad (31)$$

Denoting:

$$\frac{\partial I}{\partial x} = I_x, \quad \frac{\partial I}{\partial y} = I_y, \quad \frac{\partial I}{\partial t} = I_t \quad (32)$$

$$\frac{\Delta x}{\Delta t} = V_x \quad \frac{\Delta y}{\Delta t} = V_y$$

$$I_x V_x + I_y V_y + I_t = 0 \quad . \quad (33)$$

Here, V_x and V_y are the x and y components of optic flow (for the motion described in Fig. 14). The equation can be written more compactly as

$$(I_x, I_y) \cdot (\vartheta_x, \vartheta_y) = I_t \quad (34)$$

$$\nabla I \cdot \vartheta = -I_t \quad (35)$$

where $\nabla I = (I_x, I_y)$ is the spatial intensity gradient and $\vartheta = (\vartheta_x, \vartheta_y)$ is the velocity of the pixel (x,y) at time t. Equation 35 is called the 2-D motion constraint equation. This equation has 2 unknowns $(\vartheta_x, \vartheta_y)$, which relates to the aperture problem. If the motion detector's aperture is much smaller than the contour it observes, it can only be sensitive to the component of the contour's motion that is perpendicular to the edge of the contour. It is blind to any motion parallel to the contour. This is because the movement in this direction will not change the appearance of anything within the aperture. To find optic flow vectors, additional equations are needed. Many optic flow computation methods focus on additional constraints that attempt to recover the optic flow vectors. Lucas and Kanade⁴⁸ assume that the displacement of the image contents between 2 frames is constant within a neighborhood of a point under consideration. Horn and Schunck⁴⁹ assume smoothness in the flow over the whole image and prefers solutions that show more smoothness.

For the Lucas–Kanade motion algorithm,⁴⁸ the 2-D motion constraint equation is assumed to hold for all pixels within a window centered at p. This means that the motion constraint equation holds for all the pixels in a window with the same unknowns $\vartheta = (\vartheta_x, \vartheta_y)$. This set of equations brings an overdetermined system that has more equations than unknowns:

$$\begin{aligned} I_x(q_1)\vartheta_x + I_y(q_1)\vartheta_y &= -I_t(q_1) \\ I_x(q_2)\vartheta_x + I_y(q_2)\vartheta_y &= -I_t(q_2) \\ \dots \dots &\quad \dots \dots \quad \dots \dots \\ \dots \dots &\quad \dots \dots \quad \dots \dots \\ \dots \dots &\quad \dots \dots \quad \dots \dots \\ I_x(q_n)\vartheta_x + I_y(q_n)\vartheta_y &= -I_t(q_n) \end{aligned}$$

where q_1, q_2, \dots, q_n are the pixels inside the window. In matrix form:

$A\vartheta = b$, where

$$\begin{aligned} A &= \begin{bmatrix} I_x(q_1) & I_y(q_1) \\ I_x(q_2) & I_y(q_2) \\ \vdots & \vdots \\ I_x(q_n) & I_y(q_n) \end{bmatrix} \\ \vartheta &= \begin{bmatrix} \vartheta_x \\ \vartheta_y \end{bmatrix} \\ b &= \begin{bmatrix} -I_t(q_1) \\ -I_t(q_2) \\ \vdots \\ -I_t(q_n) \end{bmatrix} \end{aligned}$$

Least squares principle can be applied to solve this overdetermined system:

$$A^T A \vartheta = A^T b \quad (36)$$

$$\vartheta = (A^T A)^{-1} A^T b \quad (37)$$

$$\begin{bmatrix} \vartheta_x \\ \vartheta_y \end{bmatrix} = \begin{bmatrix} \sum_i I_x(q_i)^2 & \sum_i I_x(q_i)I_y(q_i) \\ \sum_i I_y(q_i)I_x(q_i) & \sum_i I_y(q_i)^2 \end{bmatrix}^{-1} \begin{bmatrix} -I_x(q_i)I_t(q_i) \\ -I_y(q_i)I_t(q_i) \end{bmatrix}. \quad (38)$$

Optic flow vectors ϑ_x and ϑ_y are searched in a tracking window, and the best match is found using the least squares method. This system is solvable if $A^T A$ is invertible. The eigenvalues of $A^T A$ (λ_1, λ_2 where $\lambda_1 > \lambda_2$) should not be too small, and $A^T A$ should be well-conditioned ($\frac{\lambda_1}{\lambda_2}$ should not be too large), so $\lambda_1 > \lambda_2$ should be somewhat similar to each other in magnitude. In other words, very small eigenvalues are interpreted as “flat surfaces”, and eigenvalues $\lambda_1 \gg \lambda_2$ or $\lambda_1 \ll \lambda_2$ are interpreted as “edges”. Optimum eigenvalues should be large enough and have similar amplitude.⁵⁰

One drawback of the Lucas–Kanade algorithm is that it theoretically fails for large motions. If the motion is too large, higher order terms may dominate Eq. 29 (the first-order Taylor Series Expansion). Reducing the image resolution may solve this issue. A pyramidal approach is available to convert large motions to small motions.⁵¹

Different optic flow computation methods can be described as either “dense” or “sparse.” From a performance point of view, dense computation methods (e.g., Horn and Schunck⁴⁹ and Farnebäck⁵²) that process all of the pixels in the image are slow for real-time applications. Instead, sparse techniques (i.e., Lucas and Kanade⁴⁸) only process the pixels of interest. For real-time applications that use optic flow computation to feed the current state of an object back to a control loop, sparse techniques may be preferred over dense techniques due to faster computational performance (and, thus, higher sampling rate). In practice, we achieved 60 frames per second (fps) using the Lucas–Kanade algorithm but only 13 fps for the Farneback algorithm (376×240 pixels 8-bit monochromatic image sequence). For this work, the Lucas–Kanade algorithm is used with predefined feature points distributed over the imagery. The feature points are the center pixel points to run the Lucas–Kanade algorithm for determining an optic flow vector. As the number of feature points increases, so does the number of optic flow vectors. The x-component of optic flow vectors are summed to obtain a single optic flow value.

3.5 Experimental Setup

In general, from Fig. 12, the optic flow experienced by an imager is³³

$$Optic\ Flow = -\omega + (V/D) \cos\theta \quad (39)$$

where ω is the angular velocity and V is the translational velocity of the vehicle, D is the distance to an object, and θ is the angle between direction of travel and direction of object. If the translational component (V) is zero, optic flow is proportional to the angular velocity.

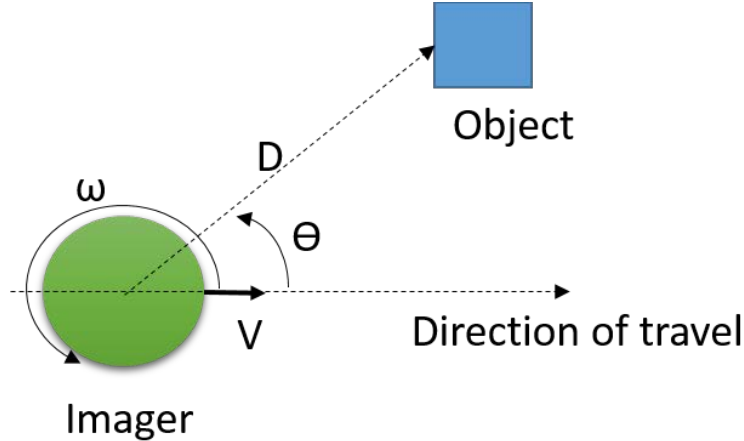


Fig. 12 Optic flow during rotational and translational motion: without translational component (V), optic flow is an estimate of only angular velocity (ω)

A mechanism was constructed to characterize optic flow and ocellar sensor over 0.1–10 Hz rotational mechanical input. Figure 13 shows the illustration of the test setup; Fig. 14 shows the scene the camera sees; Table 3 shows the system components; and Figs. 15 and 16 show the general and close-up views of the components. The block diagram of the system is shown in Fig. 17.

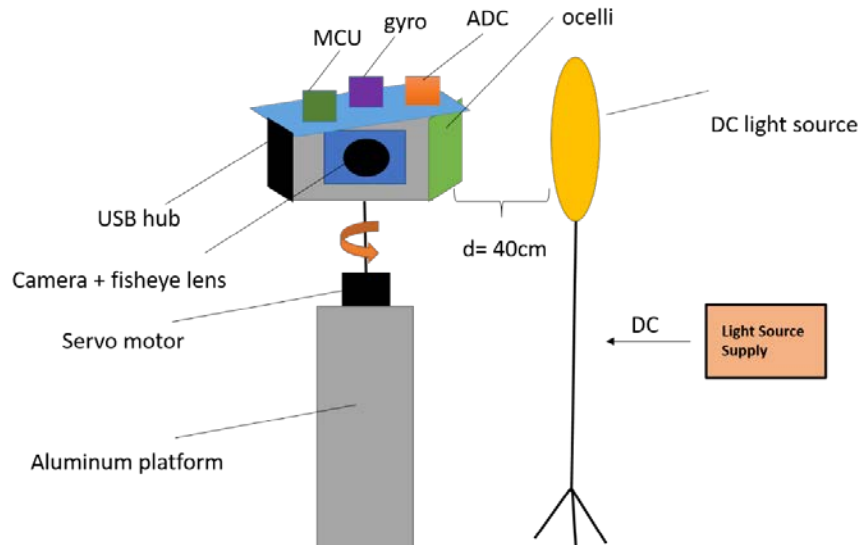


Fig. 13 Illustration of test setup: Light source has its own DC supply to avoid issues of flickering; information from camera, microcontroller unit (MCU), gyro, and analog-to-digital converter (ADC) are transferred to the host computer via a USB hub.



Fig. 14 Camera scene (376 × 240 pixel image): DC light source is not in the FOV of the camera, which is moving along the x-direction

Table 3 Experiment components

Equipment	Model/manufacturer
Light source	LED1 OOWA-56 LED Video light
Light-source supply	GW-Instek-PSW-8027 Programmable switching DC power supply
Motor	Animatics Smartmotor SM2340D
Motor supply	PS42V6AG-110, 251 W, Moog, Animatics
Signal generator	Tektronix AFG3252
Camera	UEYE UI-1221LE-M-GL USB 2.0, 752 × 480, CMOS mono, 87.2 fps, 8-bit
Lens	Sunex DSL227 Miniature superfisheye lens, 180° FOV
Microcontroller	Arduino UNO
ADC	MCP3008 8-channel 10-bit ADC with serial peripheral interface (SPI)
USB hub	Hosa Technology
Gyroscope	Pololu MinIMU-9 v3 chip contains L3GD20H 3-axis gyro

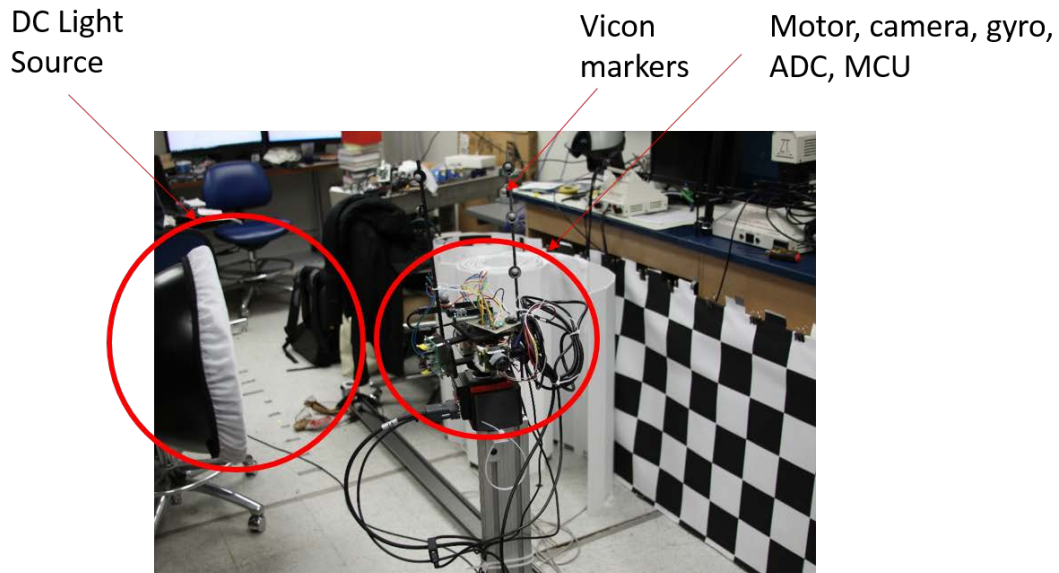


Fig. 15 Overall test setup: Ocular sensor is positioned in front of light source. Motor is giving rotational motion to the setup along its shaft axis. The motor shaft is in vertical orientation, moving the components on it.

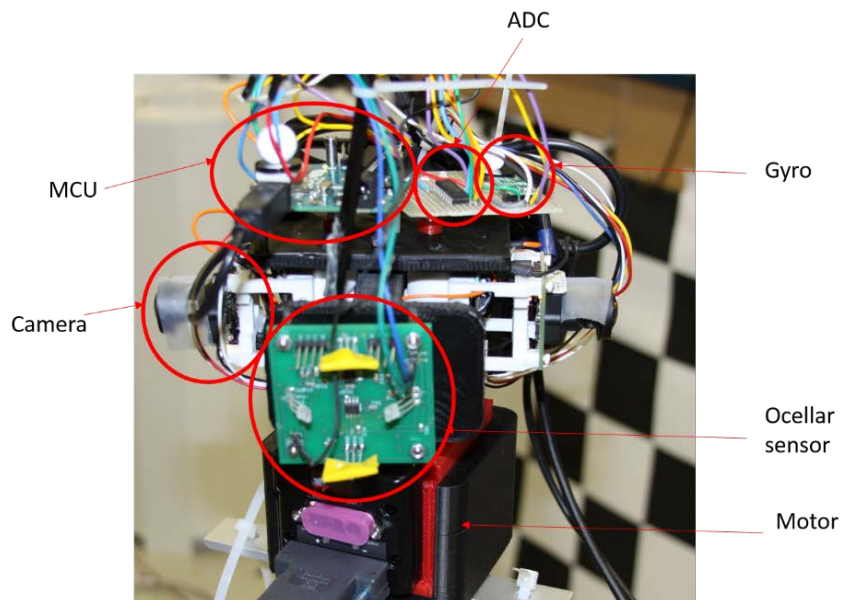


Fig. 16 Test setup components: Camera sees the scene shown in Fig. 17. Camera on the right is not used due to performance issues.

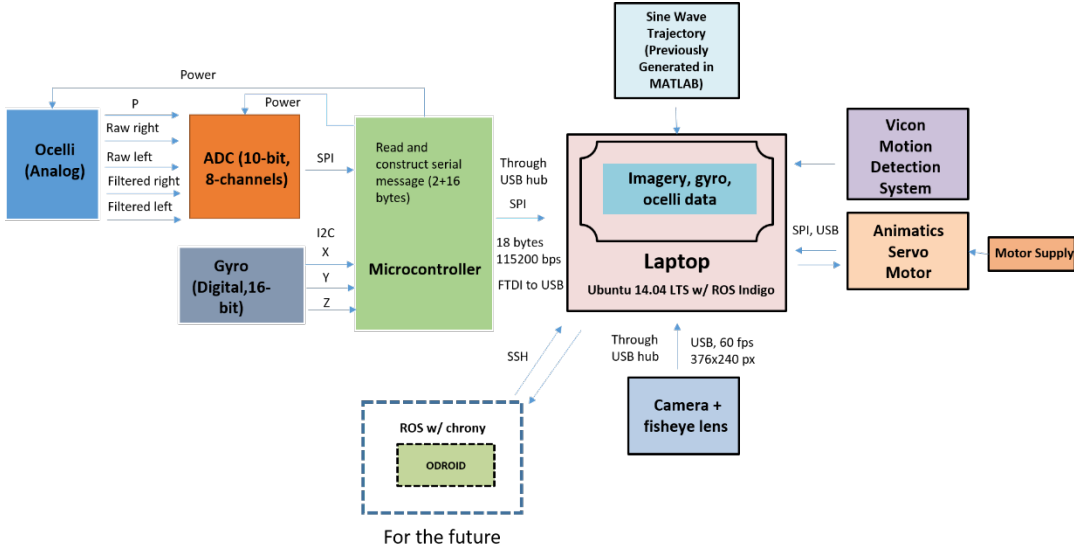


Fig. 17 System block diagram: All of the data collected are stored in laptop

All data are stored in a laptop running Ubuntu 14.04 environment. The ROS environment is used to implement robot software. ROS is an open-source network for writing robot software, including a collection of tools, libraries, and conventions. It allows for compact storage and data publishing from multiple peripherals. For this system, each component is represented by a different ROS “node” that allows for the compilation of multiple C++ files and stores data in a “bag” file. Once the data are collected, the bag file is “unbagged” and parsed to extract the data.

To record the ocellar sensor analog voltage outputs, an ADC board is used. For ground truth, a 16-bit gyroscope is also used. The ADC board (MCP3008) communicates with the Arduino UNO microcontroller via SPI. Gyroscope communication is through interintegrated circuit technology (I²C). The microcontroller is programmed in C language. It reads ADC and gyroscope outputs, and parses the values into most significant (MSB) and least significant (LSB) bytes. Each sample consists of one MSB and one LSB (i.e., a 2-byte word). A message is created (see Fig. 18) with 2 header bytes to be sent to the laptop via serial communication at 115200 bps. A 15-ms delay is added between each byte sent to allow the receiver buffer to be cleared to avoid overwriting.

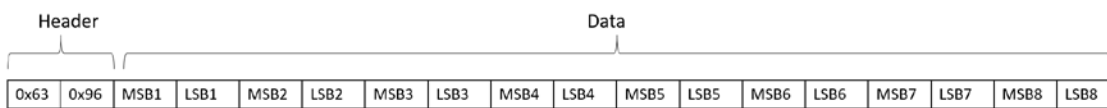


Fig. 18 Serial message structure from ocelli to microcontroller includes 2 header, ocelli data, and gyro data bytes

The servo motor can be operated in either position or velocity mode. Velocity mode does not offer control in position. The motor is controlled by sending serial messages in Ani-Basic language. (The command information and serial communication are specified in the developer's guide.⁵³) For both position and velocity modes, specific trajectory files are created in MATLAB, including velocity/position trajectory (e.g., sine wave, square wave) and acceleration information. These trajectories are recorded as text files and read by a C++ code that communicates with the motor in Ani-Basic Language via serial communication at 115,200 bps. The commanded position, velocity, acceleration and real-time position, velocity, and acceleration values can be read back from the motor controller. Reading the motor values allowed us to validate the gyroscope output and to see whether the ocelli circuit is in desired position or not. To measure frequency response characteristics, concatenated sine waves are sent as velocity trajectory at different frequencies at velocity mode. To understand the ocellar sensor validity (explained in the next section), step inputs are sent at position mode.

After storing the gyro, ocelli, Vicon, and raw imagery data in a bag file, post-processing occurs (and is summarized in Fig. 19). Using the raw imagery in the bag file, optic flow field vectors are computed with another C++ code, using the OpenCV Lucas–Kanade algorithm. A text file is generated that includes the time stamps and optic flow x and y vectors for each image. For the other data, the bag file is unbagged and parsed to extract the ocelli, gyro, Vicon, motor data, and related timestamps. Optic flow vectors generated from the Lucas–Kanade algorithm are also parsed. The text file contains 60-fps optic flow information. To obtain lower frame rate results, the optic flow values are downsampled to factors of 60. Since we have data coming from different sources at different sampling rates, synchronization is necessary using a common time vector. A common time vector for all data is created with the lowest sampling time possible, which is the microcontroller sampling time, 0.003 s. All data are interpolated using this time vector.

Since the communication modules are developed for embedded platforms, it will not take much effort to transfer this system to onboard computers used on quadrotor helicopters (quadcopters) through Secure Shell (SSH). The time synchronization can be carried out with firmware that force ones computer's clock to follow another one (e.g., “chrony” synchronization for ROS).

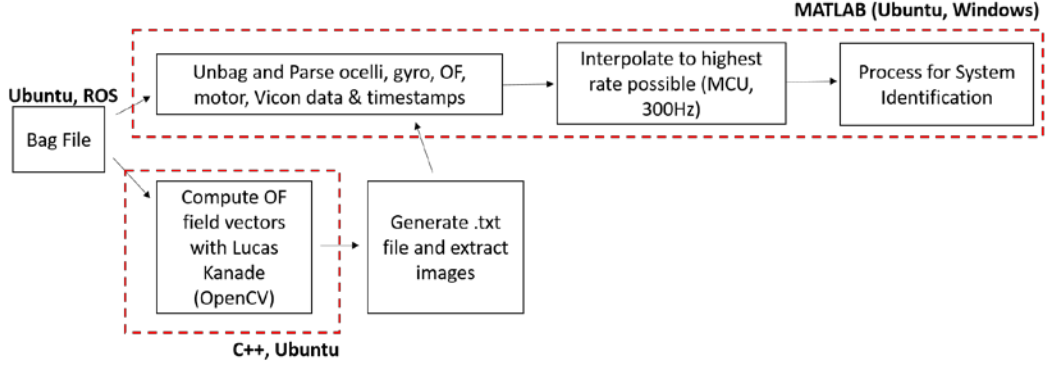


Fig. 19 Post-processing block diagram: Optic flow vectors are computed and extracted as a text file. The bag file is parsed, interpolated, and processed for data analysis.

3.6 Magnitude-Squared Coherence

The spectral coherence is a measure that can be used to examine the relationship between 2 signals (or data sets). It is commonly used to estimate the power transfer between the input and output of a linear system. The magnitude-squared coherence between two signals $x(t)$ and $y(t)$ is defined as

$$C_{xy}(f) = \frac{|G_{xy}(f)|^2}{G_{xx}(f)G_{yy}(f)} \quad (39)$$

where $G_{xy}(f)$ is the cross-spectral density between x and y , and $G_{xx}(f), G_{yy}(f)$ are the auto-spectral density of x and y , respectively. If the signals are ergodic (statistical properties can be deduced from a sufficiently long process) and the system function linear, the magnitude-squared coherence function estimates the extent to which $y(t)$ may be predicted from $x(t)$ by an optimum linear least squares function.⁵⁴ The transfer functions and operations described for the mathematical model of the system, itself, and ocellar sensor transfer characteristics are linear. Thus, we expect the system to be linear. The magnitude-squared coherence is added to the frequency response plots as a performance parameter showing linearity.

For an ideally linear system:

$$y(t) = x(t) * h(t) \leftrightarrow Y(f) = X(f)H(f) \quad (40)$$

$$G_{yy}(f) = |H(f)|^2 G_{xx}(f) \quad (41)$$

$$G_{xy}(f) = |H(f)|^2 G_{xx}(f) \quad (42)$$

$$C_{xy}(f) = \frac{|H(f)G_{xx}(f)|^2}{G_{xx}(f)G_{yy}(f)} = \frac{|H(f)G_{xx}(f)|^2}{G_{xx}(f)^2|H(f)|^2} = 1 \quad (43)$$

where $h(t)$ is the impulse response and $H(f)$ is its Fourier transform.

Values of coherence satisfy $0 \leq C_{xy}(f) \leq 1$. If there is a perfect linear relationship between x and y at a given frequency, $C_{xy}(f) = 1$. If C_{xy} is less than one but greater than zero, it is an indication that either noise is an inherent component of the system measurement, that the assumed function relating $x(t)$ and $y(t)$ is not linear, or that $y(t)$ is producing output due to input $x(t)$ as well as other inputs. If the coherence is equal to zero, it is an indication that $x(t)$ and $y(t)$ are completely unrelated.

In the physical world, a perfect linear relationship is rarely realized. In practice, coherence values higher than 0.5 are acceptable for testing linear systems. For the experiments described later, the coherence values dip down at specific frequencies, around 1–2 Hz, for all measurements. Although the input sine waves includes these frequencies, it is believed that the motor was not successful at implementing these frequencies. All of the final measurements include coherence values higher than 0.5 to be in a practically acceptable region.

3.7 Ground Truth

The first consideration for ground truth was the Vicon motion-detection system. However, its cameras strobe at frequencies 50–100 Hz and use reflected infrared light that is strobed from a ring of light-emitting diodes (LEDs) surrounding each camera. The bandpass filter circuit is able to pick up these frequency components of the infrared light, resulting in the corruption of the output signal. Alternative ground-truth options are the velocity readout from the servo motor controller and the gyroscope sensor. To choose one as ground truth, a chirp signal between 0.1 and 10 Hz was given to the motor as velocity input, and the comparative responses of motor velocity readout and gyroscope were verified, with respect to the Vicon system as input. The ideal response should be a flat curve. As seen in Fig. 20, the gyroscope provides a more flat magnitude very close to 0 dB, and less phase delay than motor velocity. The magnitude-squared coherence plot indicates a linear input–output relationship at an existing frequency. The gyroscope coherence is higher than motor velocity across all test frequencies; therefore, it is regarded as ground truth for further analysis. The curves are shown up to 15 Hz to show the coherence decay outside the test frequencies.

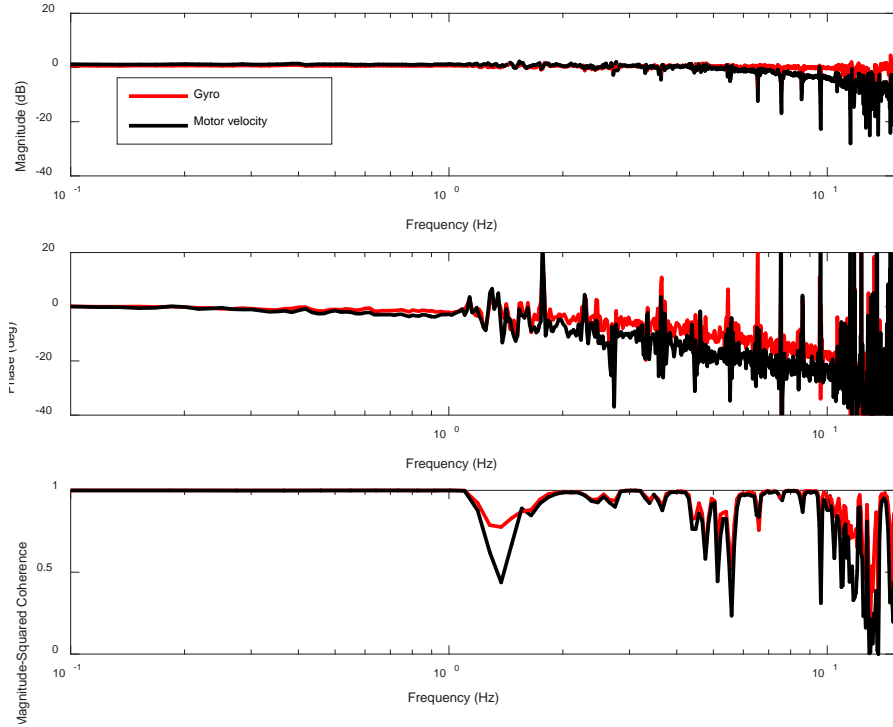


Fig. 20 Motor velocity and gyro frequency response, as seen by Vicon motion-detection system as input: Frequencies after 10 Hz were shown to prove the decrease in coherence out of controlled motion frequencies. Gyroscope shows a flatter magnitude response and higher coherence than motor velocity; therefore, it was chosen to be the ground truth.

3.8 Understanding Ocellar Sensor's "Valid Range"

The ocelli circuit is assumed to work under a specific luminance pattern to be an angular rate sensor. Assuming a bright sky and dark ground, when the photodiodes are looking to the sides, each of them sees a different horizon. One photodiode sees a brighter patch, while the other one sees a darker patch. For this algorithm to work, the luminance gradient from the sky to the ground should be constant and negative. We use a light source with a diffuser to create this artificial sky and horizons. The diffuser prevents the direct current (DC) source from acting as a point source, by helping to distribute the light intensity along the diffuser surface. This way, the light source acts as the sky, rather than the Sun. The photodiodes should see the 2 edges of the source as 2 horizons. This way, when a rotational motion is applied, brighter-darker patch assumption will be satisfied. The photodiodes should be bent towards the source to intersect their fields of view. To understand whether an intersection is created, the azimuthal position of the motor is varied and the photodiode outputs are checked to see if they share an overlapping FOV. Figures 21 and 22 show the unbent and bent raw photodiode outputs, with respect to the azimuthal position of the motor. A partially overlapping FOV was achieved by bending the photodiodes toward the light source.

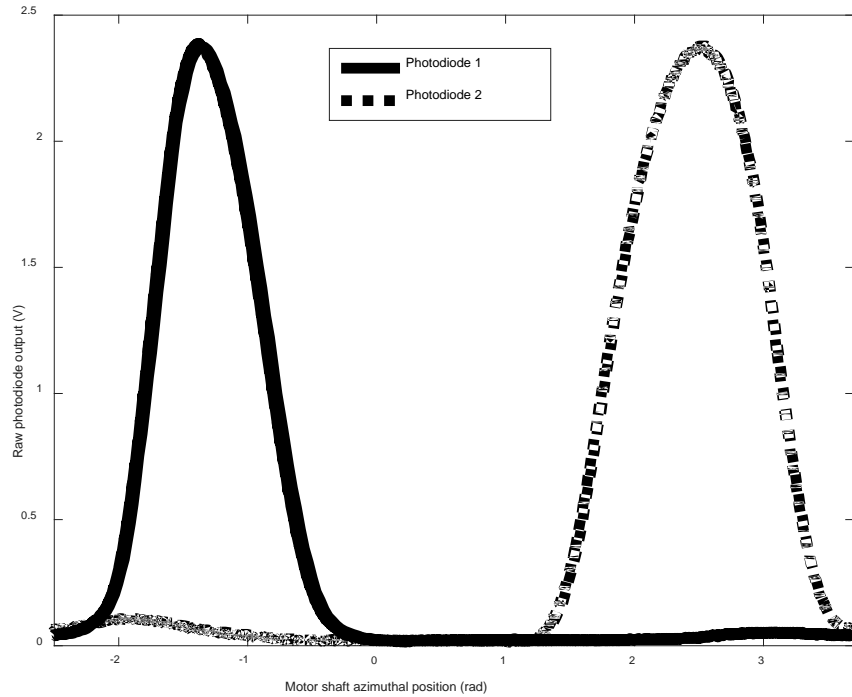


Fig. 21 Unbent photodiode output vs. motor shaft azimuthal position: Photodiode outputs increase as they pass by the light source. FOVs are not overlapping.

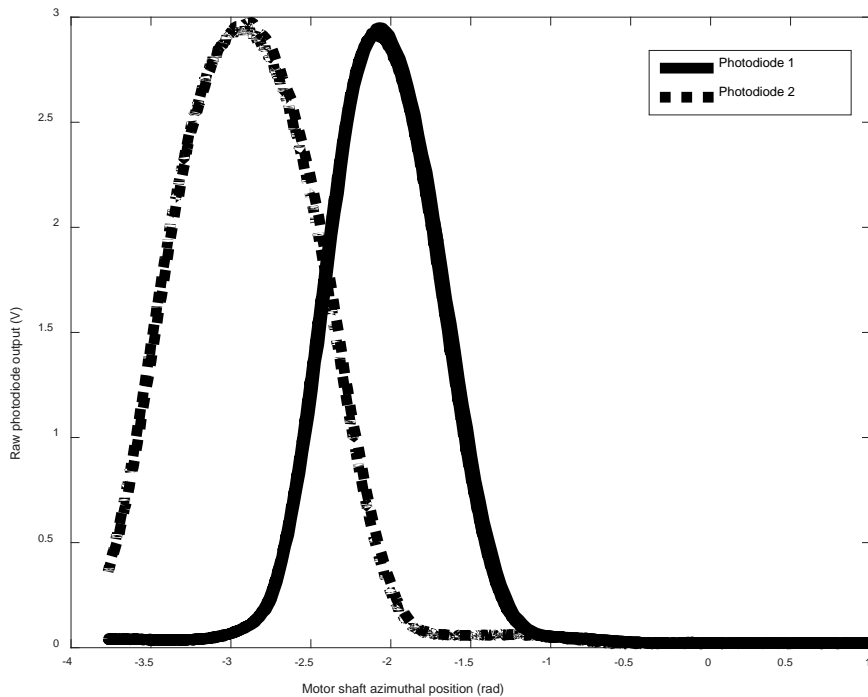


Fig. 22 Bent photodiode output vs. motor shaft azimuthal position: Photodiode FOVs are partially overlapping, which is required for the ocellar sensor to work. In this (incorrect) configuration, there are angles where simulated roll motions do not produce any change in the photodiode outputs.

Due to the small size of the light source and small FOV of the photodiodes (around 90° each), the maximum swing of the motion stimulus needs to be small enough to ensure that the photodiode outputs are changing symmetrically with respect to each other. To understand the dynamic range circuit's velocity, the azimuth was varied with small steps. For each position value, a target velocity was given to the motor and the circuit output was compared to the gyro output. For the region outside the light source dominance, the circuit outputs are not reliable.

Figure 23 shows a valid region (azimuthal position changes from -0.2 to 0.2 radians). In this range, photodiode outputs are symmetric to each other and the ocelli output directionally matches the gyro output.

Figure 24 shows an invalid region (azimuthal position changes from -1.4 to -0.2 radians). In this range, photodiode outputs are not symmetric to each other. Ocelli is not in agreement with gyro. Using this data, the maximum displacement for the ocellar circuit is determined to be 1 radian. All of the following characterizations are done in this valid region.

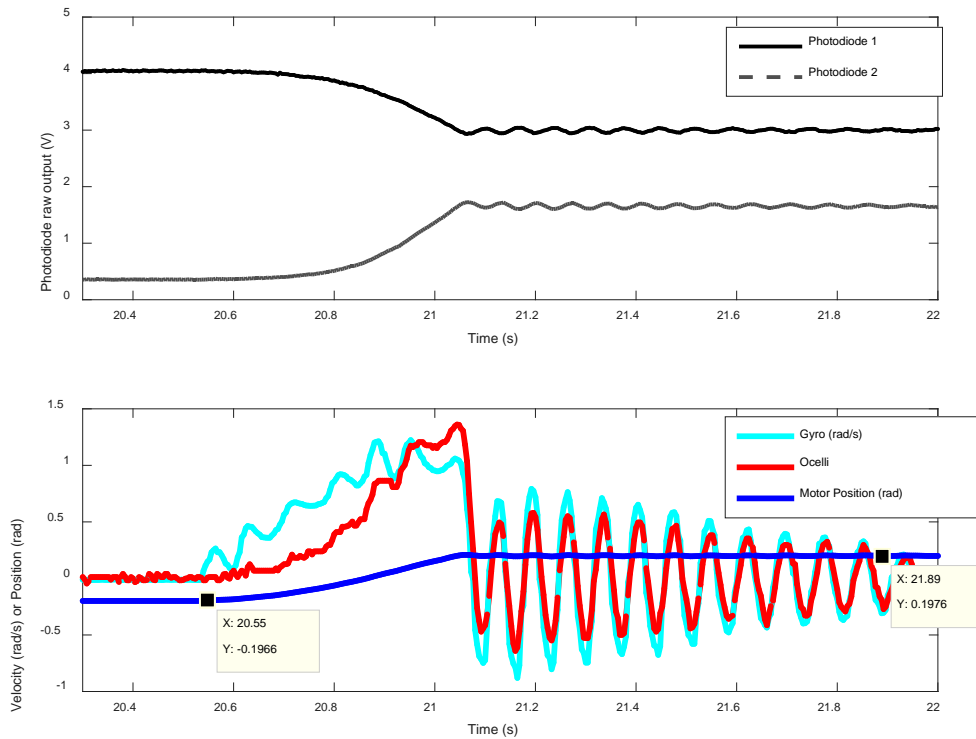


Fig. 23 Ocelli in valid range: (above) symmetric photodiode raw output; (below) gyro and ocelli output for motor azimuthal position (-0.2 to 0.2 radians). Ocelli output is in agreement with gyro in this range.

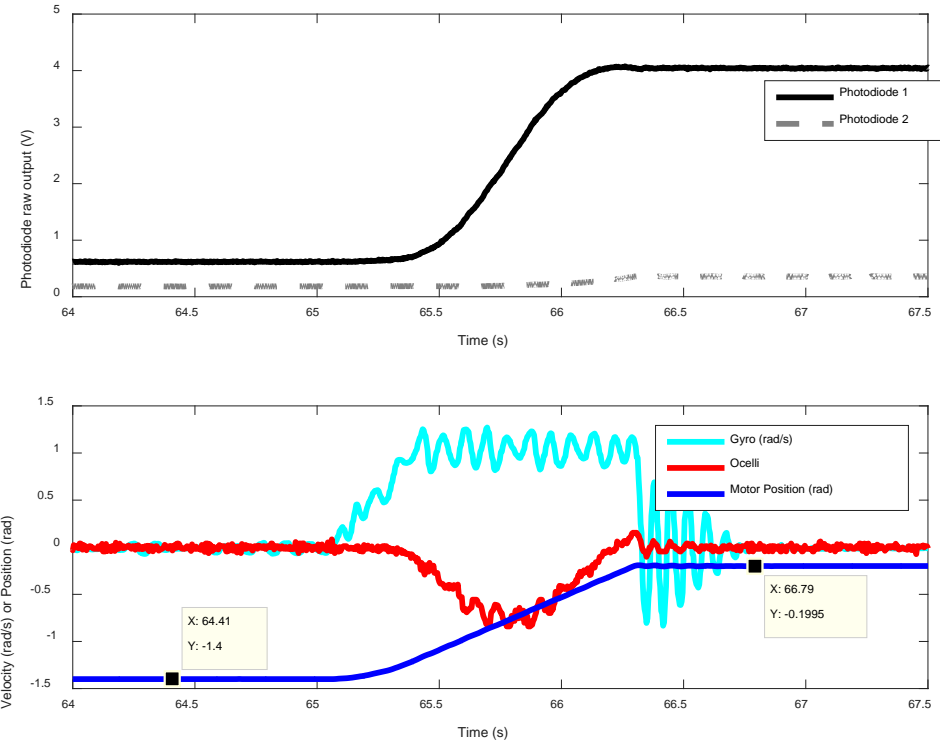


Fig. 24 Ocelli in invalid range: (above) asymmetric photodiode raw output; (below) gyro and ocelli output for motor azimuthal position (-1.2 to 0.2 radians). Ocelli output is not in agreement with gyro in this range.

3.9 Ocellar Sensor Frequency Characterization

Frequency characterization is done in 2 ways. First, to confirm the proper operation of the bandpass circuit, the raw photodiode output is used as input and filtered signal is used as output. Although the bandpass circuits can operate up to higher frequencies, the motor stimulus is limited to 10 Hz; only 0.1–10 Hz data are obtained for circuit’s motion characterization. To demonstrate that the photodiode and bandpass filter combination can operate at higher frequencies, an LED was driven by a signal generator between 3 and 100 Hz.

A second frequency characterization was done to compare the optic flow and ocelli outputs with the gyro as ground truth. This provided us with information about how well the sensors operate within the motion frequencies, in comparison to each other with the same inputs.

3.9.1 Circuit Frequency Characterization

A chirp signal is given as a motor velocity command. Figure 25 shows the simulated circuit output, and Fig. 26 shows the right and left circuit frequency responses. Between 0.1 and 10 Hz, the circuit simulation shows 20 dB/decade increase in

magnitude, starting from -38 dB to 1 dB. The phase delay starts from -90° and reaches to -125° at 10 Hz. The data from both photodiodes show the similar response. Right-circuit magnitude starts from -38 dB and reaches to -2 dB. Left-circuit magnitude starts from -38 dB and reaches to 0 dB. Phase response reaches to -140° and -124° for right and left, respectively, after starting from -90° .

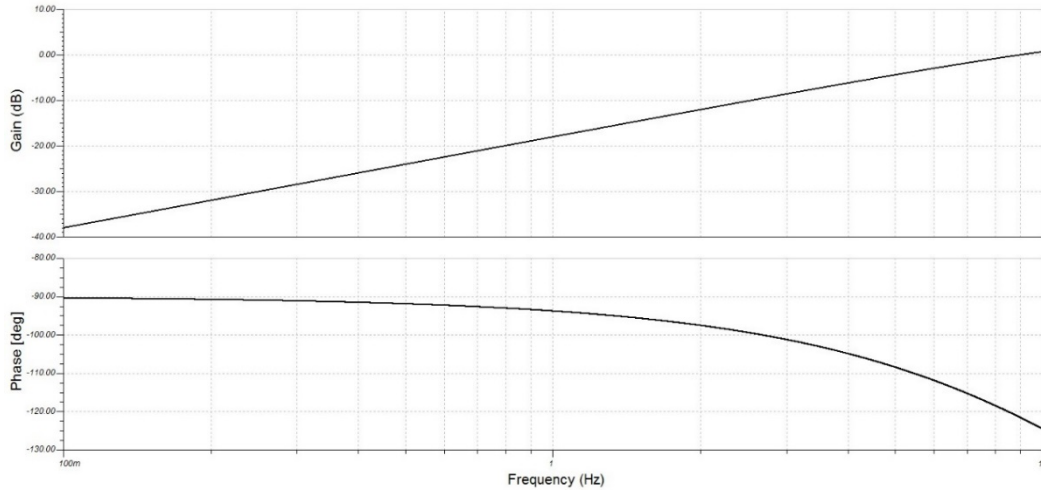


Fig. 25 Band-pass filter simulated AC transfer characteristic at $0.1\text{--}10$ Hz: Magnitude increases with 20 dB/decade. Phase drops from -90° to -125° at the end of 10 Hz.

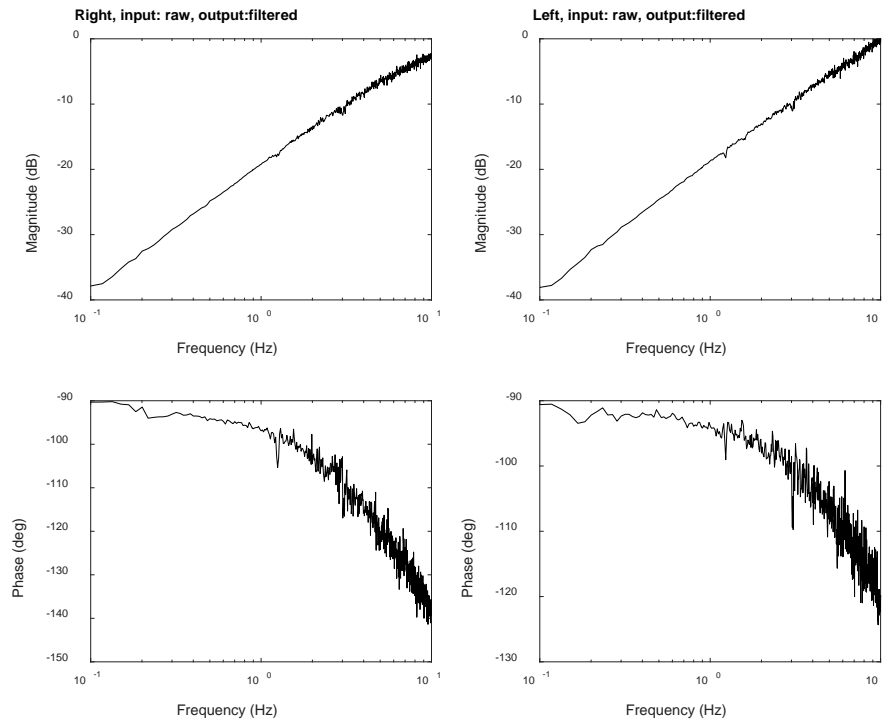


Fig. 26 Right and left band-pass filter measured AC transfer characteristics at $0.1\text{--}10$ Hz: Magnitude and phase plots are in agreement with simulation (Fig. 28).

To demonstrate that the photodiode and bandpass filter combination can operate at higher frequencies, an LED was taped to one photodiode (see Fig. 27). The electrical signal (sine wave, voltage-controlled) from the signal generator is swept from 3 to 100 Hz. Figure 28 shows the AC characteristics simulation from 3 to 100 Hz. The gain starts from -8.59 dB and reaches to 5.6 dB at 50 Hz, then it decreases to 4.74 dB at 100 Hz. The phase starts from -101° at 3 Hz, decreasing to -205° at 100 Hz. Figure 29 shows the frequency response of the circuit from the photodiode input from LED to the filtered output. The magnitude response starts from -10.25 dB and reaches to -0.29 dB at 50 Hz. Then it decays to -1.281 dB at 98.6 Hz. The phase response starts from -105.8° at 3 Hz, decreasing to -180.5° at 98.76 Hz. Qualitatively, circuit simulation is close to actual data. Circuit simulation results in 103° phase delay, and data result in 75° phase delay. The circuit gain increases by 14 dB up to 50 Hz, and real data gain increases by 10 dB.

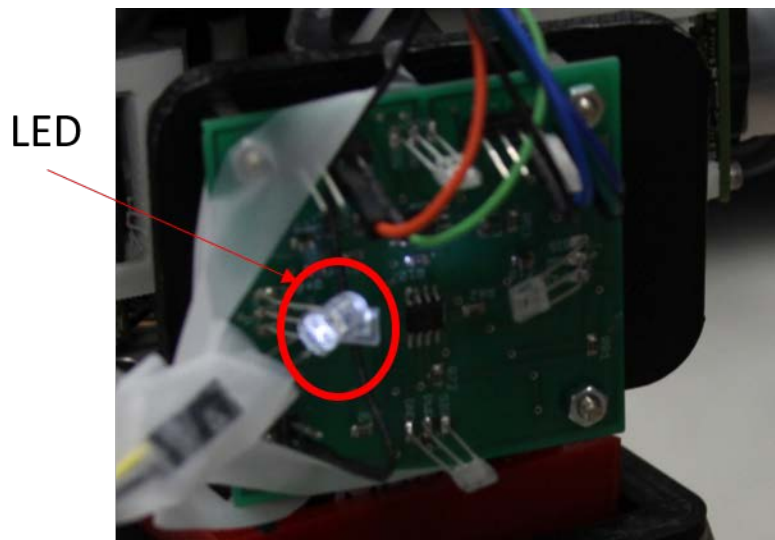


Fig. 27 LED sweeping: LED was taped to photodiode and power-supply signal is swept between 3 and 150 Hz.

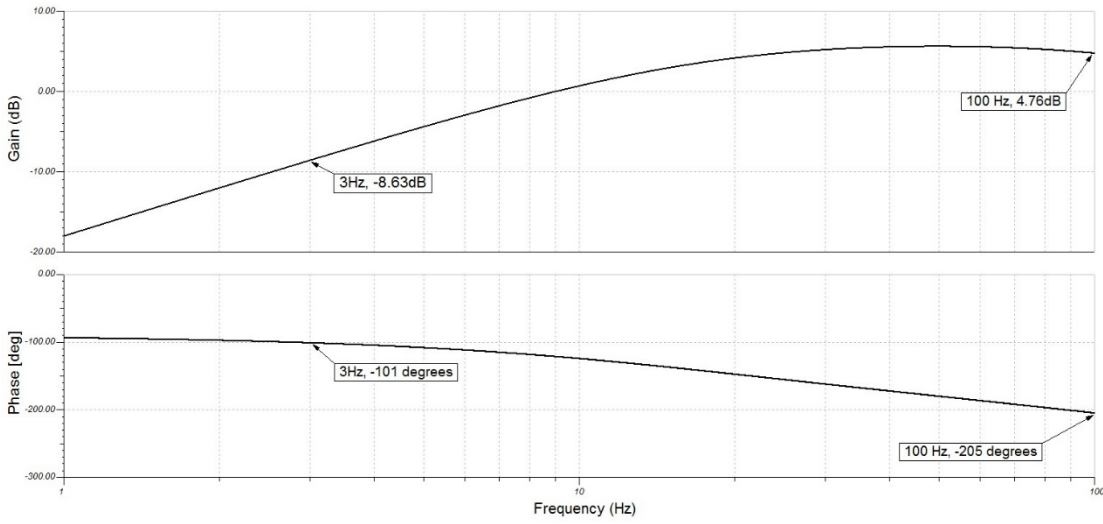


Fig. 28 Right and left band-pass filter simulated transfer characteristics between 1 and 100 Hz; simulation is shown to compare with LED sweeping results in Fig. 32

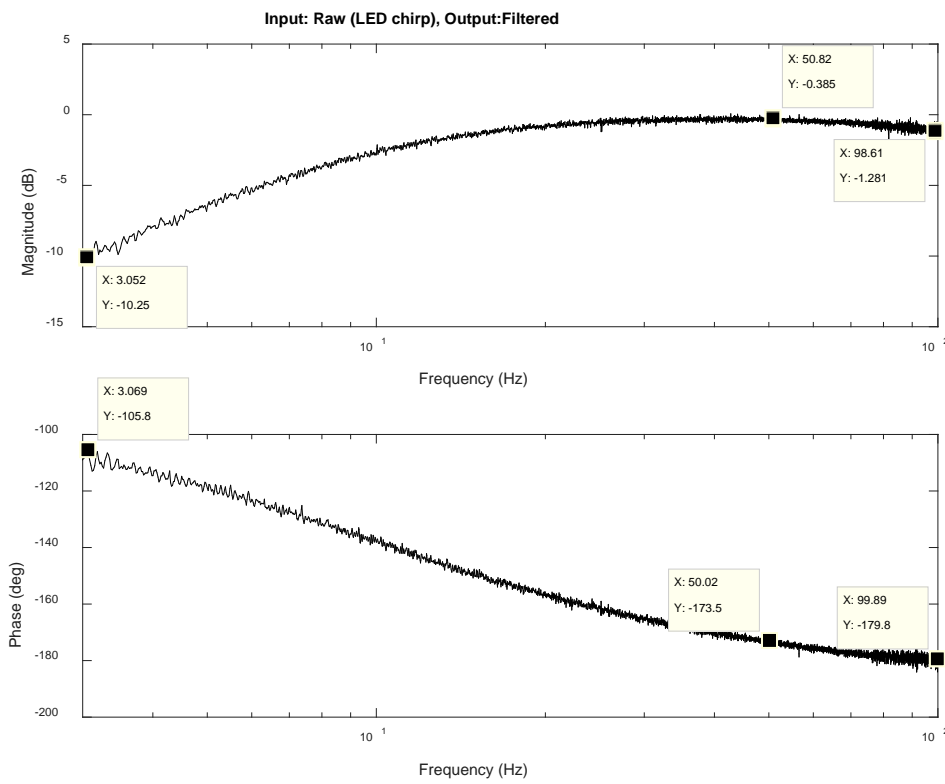


Fig. 29 Right band-pass filter measured transfer characteristics in response to LED chirp between 3 and 100 Hz: magnitude increases 20 dB/decade and phase drops from -105° to -180° (in agreement with simulation in Fig. 31).

3.9.2 Sensor vs. Ground Truth Frequency Characterization

To characterize ocellar sensor frequency response with respect to the gyroscope (acting as the ground truth velocity), concatenated sine waves were given as velocity input. The operation was performed in the valid angle range previously described. The ocelli output is a voltage value. Its magnitude is scaled to match with the gyroscope. This frequency response is from gyroscope as input, to the full ocellar sensor as output. Within the test frequencies, the ocellar sensor shows a relatively stable magnitude around 0 dB. The phase response is degrading over the frequency range. Figure 30 shows the ocelli sensor frequency response. From 0.1 to 1 Hz, there is almost no phase delay between ocelli and gyro. After 1 Hz, ocelli shows a phase delay of approximately 15°. The data after 10 Hz were not taken into account, since the input stimulus cannot exceed 10 Hz. The components at higher frequencies are due to mechanical noise inherent in the motor. Coherence dips are happening at the same frequencies with the other experiments; therefore, it is believed that the motor was not able to implement those frequency components. Ocelli always shows a coherence above 0.5, which is practically acceptable.

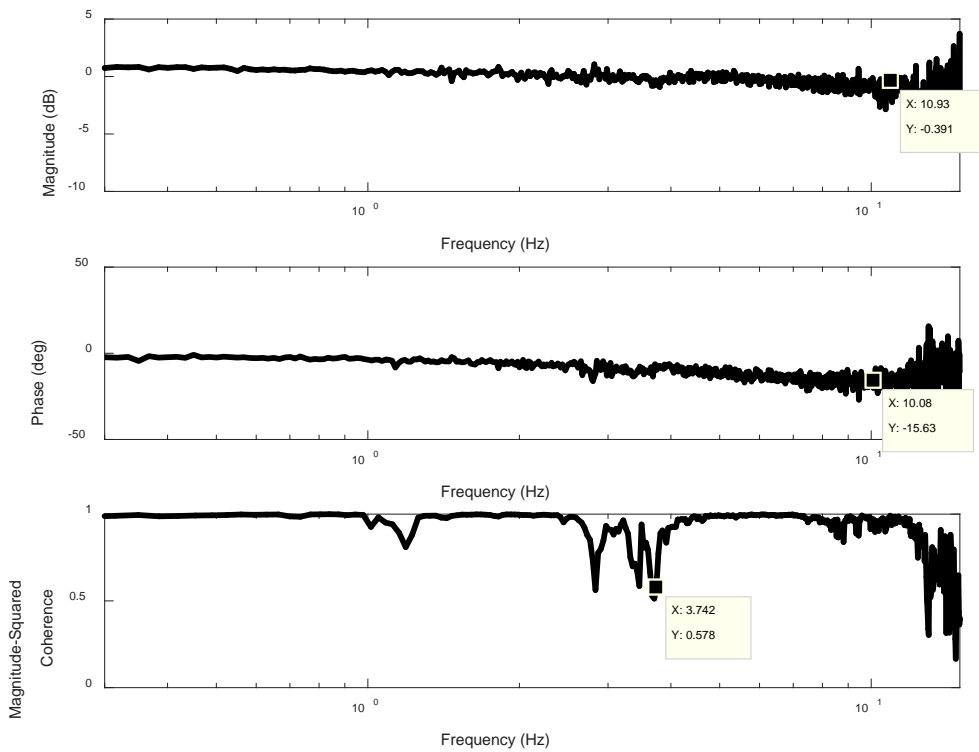


Fig. 30 Ocelli frequency response with respect to gyro as input: Frequencies after 10 Hz were shown to prove the decrease in coherence out of controlled motion frequencies. Ocellar magnitude is relatively flat, showing around 1dB difference from beginning to end. Phase delay reaches to -15° at 10 Hz.

Figure 31 shows the time-domain signals comparing gyro, ocelli, and optic flow in 0.5 Hz, 1 Hz, 5 Hz, and 10 Hz windows, respectively. The outputs of optic flow and ocelli are scaled to match gyro output (rad/s) at each window. The ocelli and optic flow are in agreement with gyro signal at each frequency window.

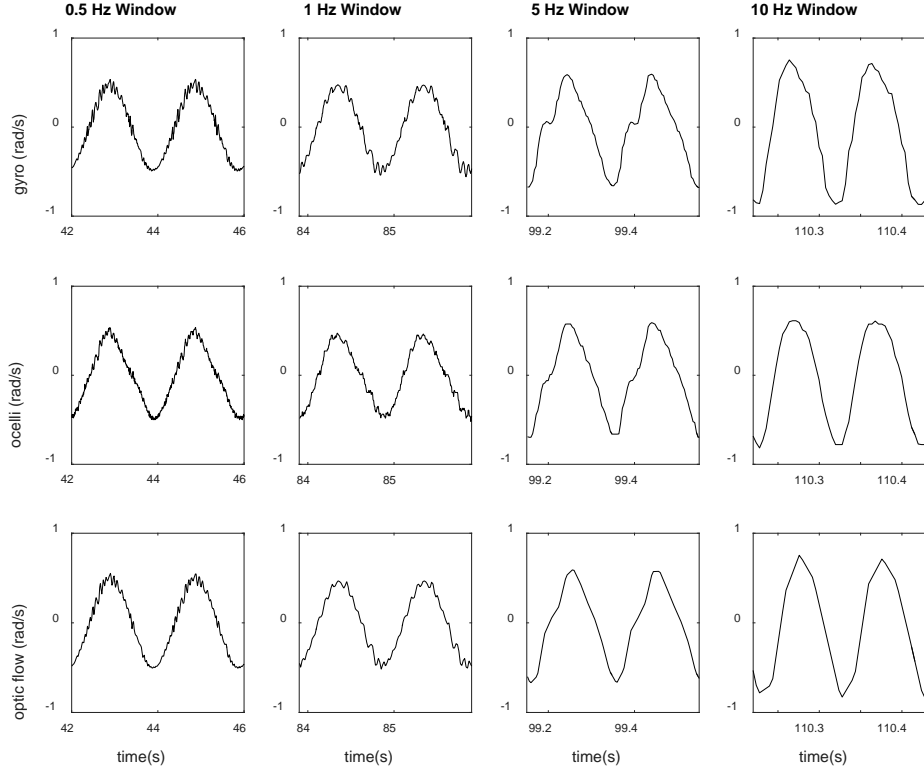


Fig. 31 Time signals of gyro, ocelli, and optic flow in 0.5-, 1-, 5-, and 10-Hz windows; all sensor outputs are scaled to match gyro (rad/s) at each window

Figure 32 shows the optic flow frequency characterization for 60 fps data, using Lucas–Kanade with 25-pixel window size and 16 feature points (4×4). The entire magnitude response is very close to flat. There is almost no phase delay until 1 Hz, at which point it reaches -35° at 10 Hz. Taking into account that these optic-flow data are obtained with the highest frame rate, the magnitude response is expected to degrade as the frame rate decreases. Although the optic flow frequency response remains approximately flat with these settings, the frequency response is related to the motion algorithm, frame rate, and window size, as will be seen next. Varying these parameters, a worse high-frequency response will be obtained, which is the real-life case with flying vehicle onboard computers. All in all, these data show the maximum bandwidth the optic flow can achieve within the test limitations.

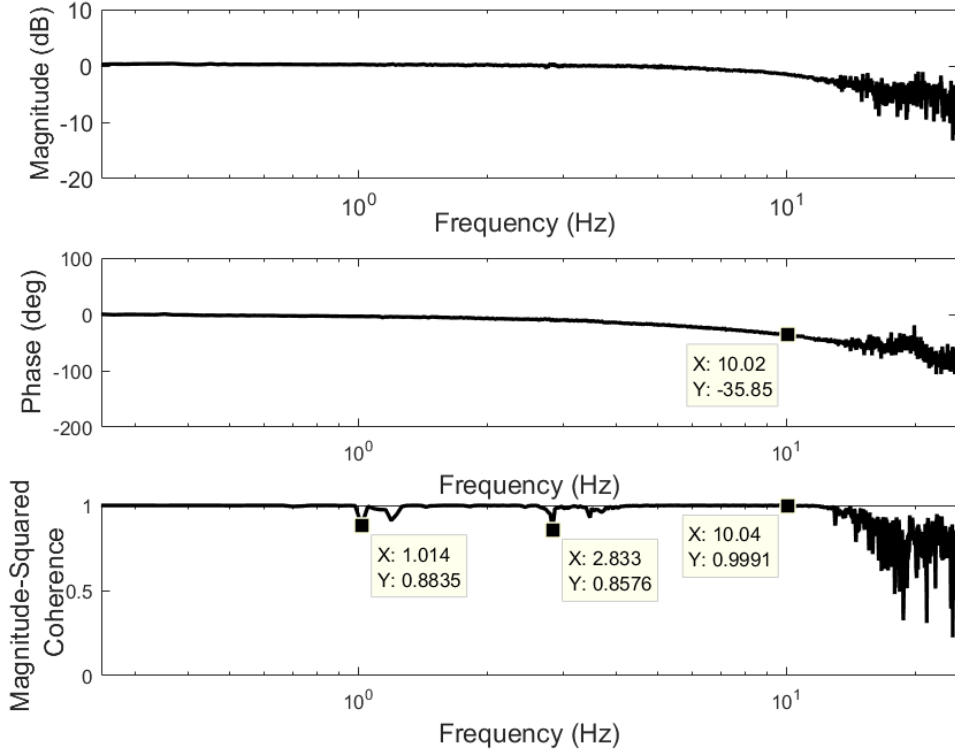


Fig. 32 Frequency response of optic flow with respect to gyro as input: Overall magnitude decrease is 1.42 dB. Phase delay reaches to -35° at 10 Hz.

3.10 Ocellar Sensor–Gyro Voltage–Velocity Mapping

To understand the expected ocelli output (in volts) for a given gyro (rad/s) value, the data for ocelli and gyro across 1–10 Hz test frequencies were combined. With 0.005 rad/s intervals, expected ocelli output (V) and gyro (rad/s) values were calculated (16 data points for both). These points were fitted to a line of equation

$$f(x) = p1 * x + p2 \quad (44)$$

where $p1 = 0.164$ and $p2 = 2.489$, $R^2 = 0.9902$. Figure 33 shows the mapping plot. It shows that the ocelli output is monotonically increasing with increasing gyro amplitude, implying linearity. The standard deviation (error bars) is large because of the discretization limit of the ADC. The ADC has 4.8 mV resolution, and the overall motion is within 140 mV.

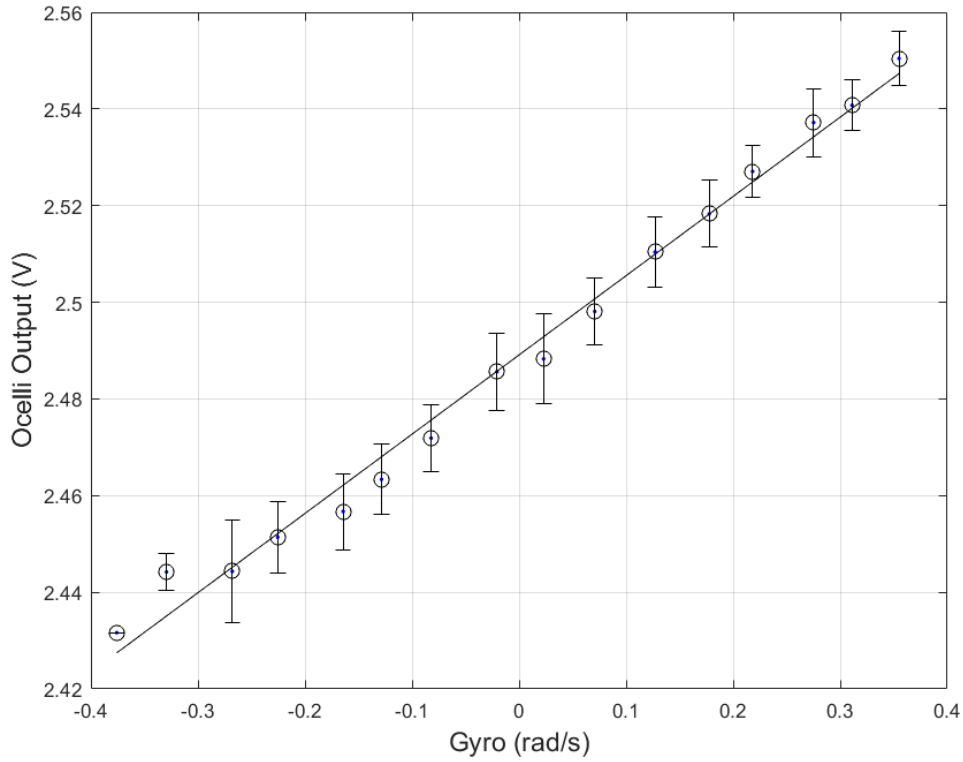


Fig. 33 Ocelli-gyro mapping plot shows the expected ocelli output (V) for a given gyro measurement (rad/s). Ocelli output is monotonically increasing with increasing gyro values.

3.11 Performance-Related Parameters

3.11.1 Frame Rate

Frame rate is the frequency at which the camera displays consecutive images. From Eq. 2, the Lucas-Kanade algorithm extensively uses spatial and temporal derivatives, using numerical differentiation. To give an example, let f be a given function that is only known at a number of isolated points. The problem of numerical differentiation is to compute an approximation of the derivative f' of f by suitable combinations of the known values of f .

Assuming that function f is differentiable, the derivative $f'(a)$ for some real number, a , is defined as

$$f'(a) = \lim_{h \rightarrow 0} \left(\frac{f(a+h) - f(a)}{h} \right) \quad . \quad (45)$$

For very small h , this derivative can be approximated by

$$f'(a) \approx \frac{f(a+h) - f(a)}{h} \quad . \quad (46)$$

This approximation involves error, and this error increases as h increases. To demonstrate this, one can use $f(x) = \sin x$, $f'(x) = \cos x$ and compute the error between $f'(x) = \cos x$ and $f'(x) \sim \frac{f(x+h)-f(x)}{h}$. The error will increase as the h values increase.

Figure 34 shows the frequency response of 60, 30, and 20 fps optic flow results from gyro as input and from optic flow as output. As frame rate decreases, optic flow magnitude response rolls off steeper and reaches to -2.64 , -4.92 , and -9.62 dB at 10 Hz for 60, 30, and 20 fps, respectively. For all frame rates, the phase delay remains constant. For 0.1–1.1 Hz, there is almost no phase delay between optic flow and gyroscope. After 1.1 through 10 Hz, the phase delay increases and reaches -35° . The coherence of 20 fps measurement is the worst, as increasing frame rate increases the coherence, as well.

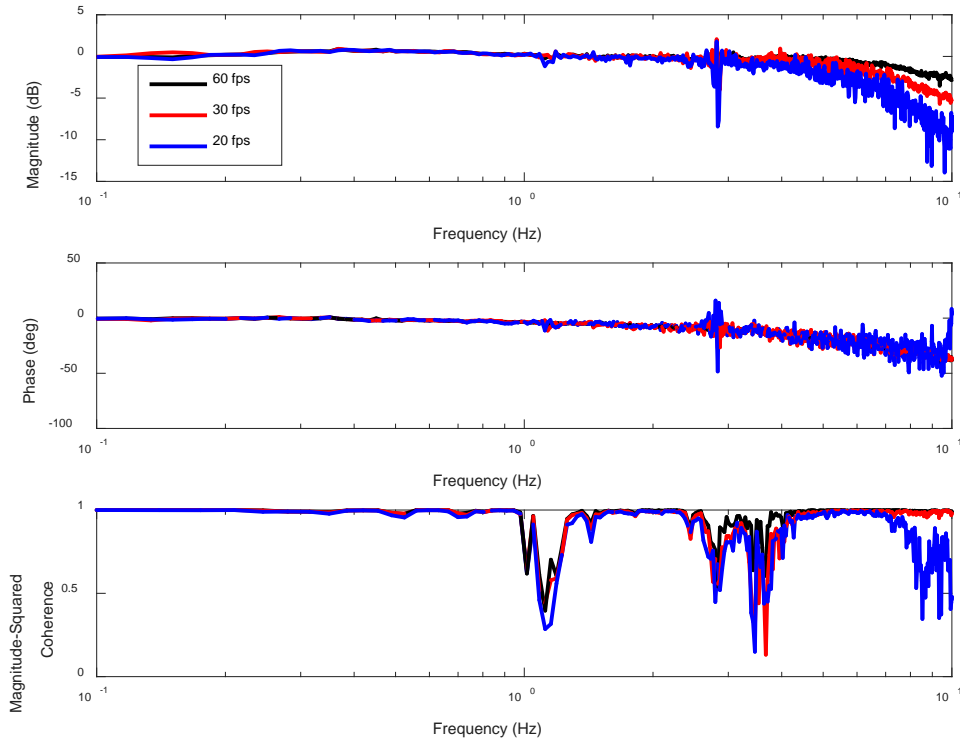


Fig. 34 Optic flow frequency response with different frame rates, as seen by input gyro: As the frame rate decreases, roll-off at higher frequencies is steeper. Higher frame rate results in better coherence. Phase delay does not change due to frame rate.

Besides numerical differentiation error, another explanation lies under the Taylor series approximation used to derive the motion constraint equation. Taking only the first-order components assumes that the change in motion is small. However, when the change is larger, the second-order components will come into play and the motion constraint equation will no longer hold. When the motion is too fast for a

given frame rate, the spatial/temporal estimate assumption breaks down. In practice, this resulted in an optical flow measurement of erroneously low magnitude.

Aliasing is another way to look at this roll-off. When the frame rate decreases, there are less optic flow vectors to sample the given sine wave. These vectors may be computed at random points of the sine wave, not exactly catching the peak amplitudes. If the frame rate is higher, more optic flow points will result in a more accurate sine wave, catching the peaks.

Scheider et al.⁵⁵ study the optic flow outputs as the angular rate changes. According to their findings for 2 different optic flow algorithms, optic flow matches with real rate for slow motions for a specific resolution. As the rate increases, optic flow cannot capture images often enough to get an accurate estimate of angular rate. Optic flow first draws a unity line with real rate, then this line starts showing a fixed rate; finally, it rolls completely off to zero.

To overcome this, one may increase the frame rate, or, use a smaller image (e.g., binned by 2) to double the frame rate. With the current setup, a 752×480 -pixel image can go up to 20 fps. When the image is binned by 2, the frame rate increases to 60 fps for a 376×240 -pixel image. This solution will result in losing maximum image resolution.

3.11.2 Window Size

The Lucas–Kanade algorithm assumes that the motion is the same for all pixels in a window of w by w pixels. This tracking window size determines the number of equations (hence, optic flow vector candidates) to be used in the least squares method. Assuming constancy in motion, more optic flow vectors will give more data points to determine the best fit for optic flow. However, if the window is too large, a point may not move like its neighbors.

Figures 35 and 36 show the window size versus the optic flow frequency response. Changing window sizes significantly affected the coherence plot. Phase delay remained the same for all window sizes. Magnitude is the most erroneous for the 10- and 20-pixel (10×10 , 20×20) window sizes; however, it stays relatively the same for the rest. The coherence is the worst using 10 pixels. It improves as the window size increases from 20 to 40 pixels, and remains the same after 40 pixels through 70 pixels.

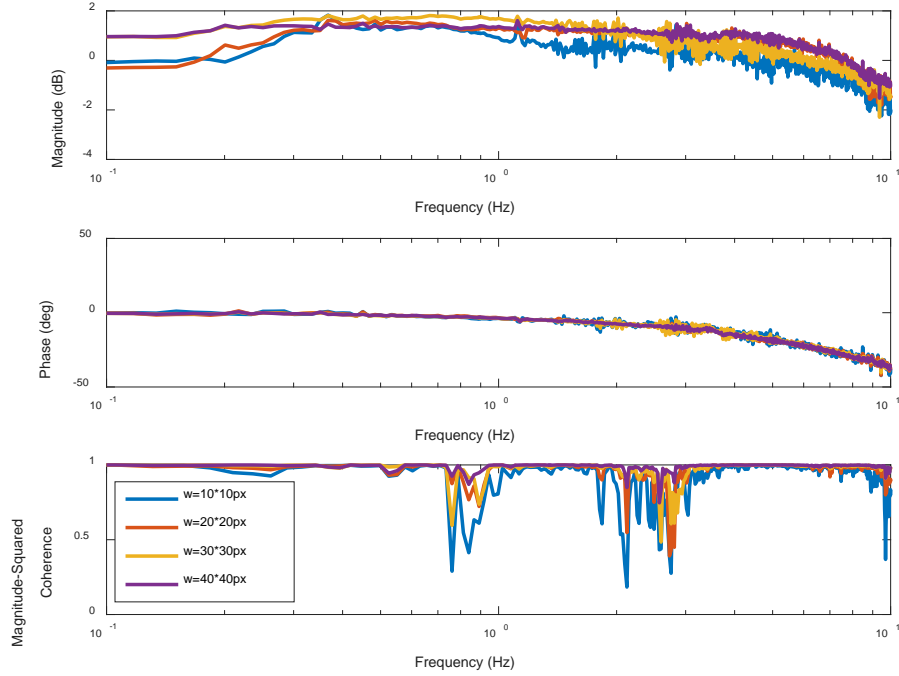


Fig. 35 Optic flow frequency response with different window sizes ($w = 10, 20, 30, 40$), as seen by input gyro: Very small windows (10×10 pixel) result in erroneous magnitude response. Magnitude response and coherence improve as window size increases, phase delay remains the same.

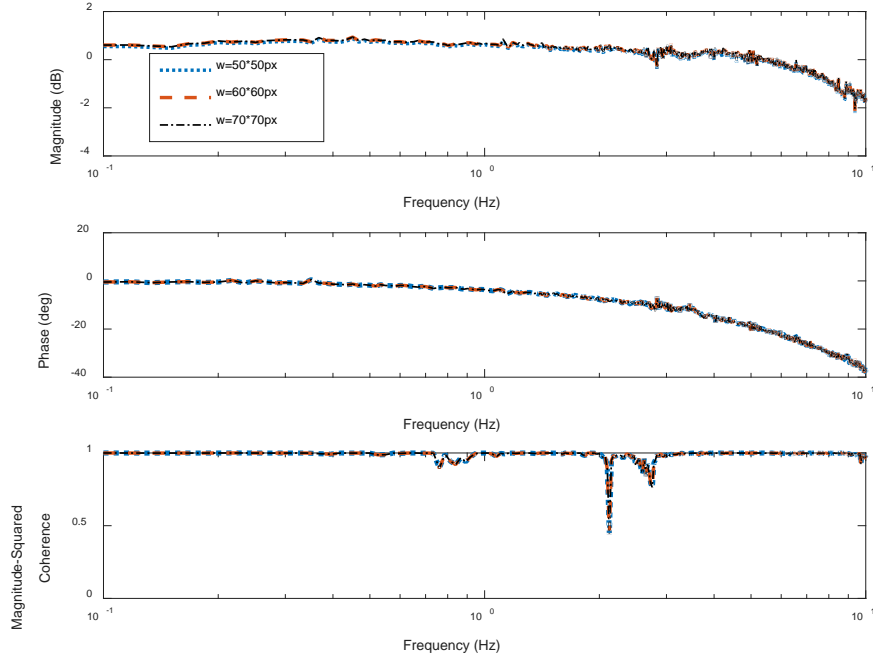


Fig. 36 Optic flow frequency response with different window sizes ($w = 50, 60, 70$), as seen by input gyro: After 50×50 -pixel window, magnitude, phase, and coherence plots do not change.

3.11.3 Feature Points

Feature points are the number of center pixels located on each image. Around these center pixels, optic flow vectors are calculated within the window size. The number of feature points determines the number of optic flow vectors computed. The plotted optic flow is only the x component of average optic flow field. The feature points are equally distributed over x and y dimensions of the image. The spacing between them is

$$x \text{ (or } y\text{) spacing} = \frac{\text{image width(or height)}}{\text{number of feature points along } x \text{ (or } y\text{)}} \quad (47)$$

where x feature points are referred to as x-by-x center pixels. Figures 37 and 38 show the image scene with 10×10 and 4×4 feature points, respectively.



Fig. 37 Camera scene (10×10 feature points)



Fig. 38 Camera scene (4×4 feature points)

Figure 39 shows the optic flow frequency response with respect to different number of future points. The 2×2 feature points result in the most erroneous optic flow magnitude. The magnitude response improves after 2×2 and stays relatively the same from 4×4 to 15×15 feature points. Similar to window size result, the change in phase remains the same between feature points. The coherence is the worst using 2×2 feature points. Increasing the feature points improves the coherence; however, coherence remains the same after 8 feature points. This means that a sufficient number of optic flow vector data points are accumulated to make the best fit for optic flow with 8×8 feature points. More feature points bring redundant data points.

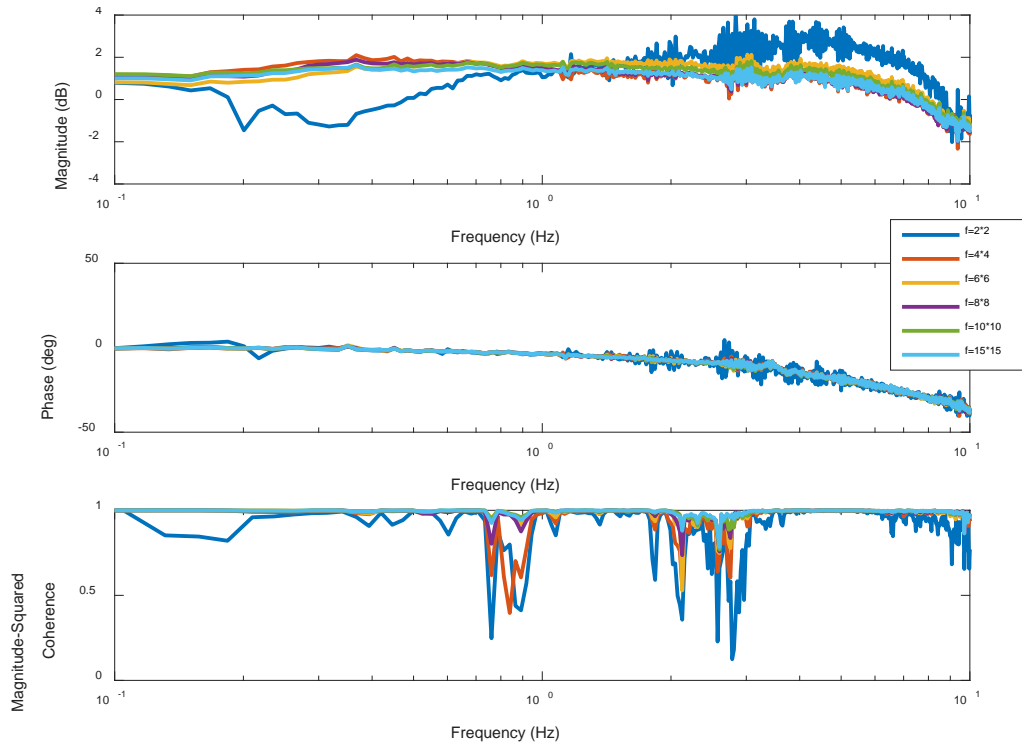


Fig. 39 Optic flow frequency response with different number of feature points (f), as seen by input gyro: 2×2 feature points result in erroneous magnitude plot. As the feature points increase, magnitude and phase plots do not show much change; however, coherence improves.

3.11.4 Luminance Intensity

DC light input power is varied to understand how the luminance intensity changes the ocellar circuit output. The circuit outputs at the same frequency were compared. Figure 40 shows the peak-to-peak amplitudes with respect to input power, for 10 Hz motion. As the power increases, amplitude increases, as expected. The fitted line has coefficients of $p_1 = 0.088$, $p_2 = 0.006$. This brings a necessity for “adaptive gain” for different luminance values in the environment.

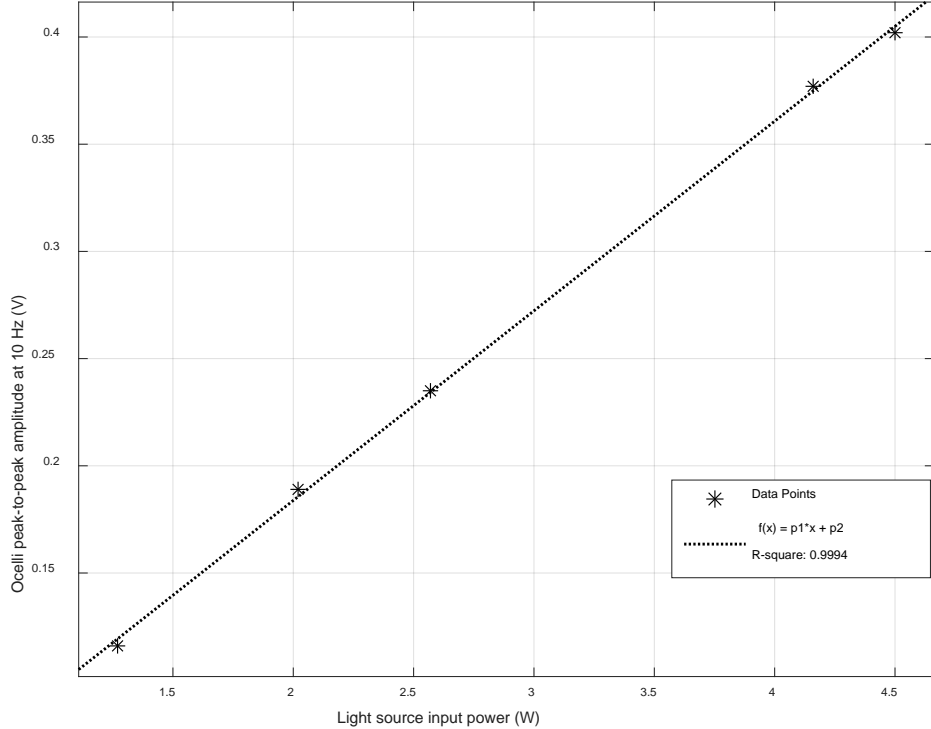


Fig. 40 Light source input power vs. ocelli peak-to-peak amplitude: Luminance increase linearly increases the peak-to-peak amplitude. DC light source is specified in Table 3.

3.11.5 Photodiode Bending

The photodiodes should be bent towards the light source to share an intersecting FOV and to satisfy that one's output is increasing while the other's is decreasing. The bending determines how much their FOVs intersect and how much they are seeing the edges of the light source as 2 different horizons. The reference for bending is seen in Fig. 41. If $\beta = 0^\circ$, no common luminance is shared. If $\beta = 90^\circ$, their FOVs completely intersect and no symmetric change with respect to each other is observed. Assumption is satisfied for β values between 0 and 45° , specifically $\beta = 30^\circ, 40^\circ, 45^\circ$ raw outputs are observed to be symmetric to each other. For $\beta \sim 90^\circ$, the same sine wave shape is seen at the same instant.

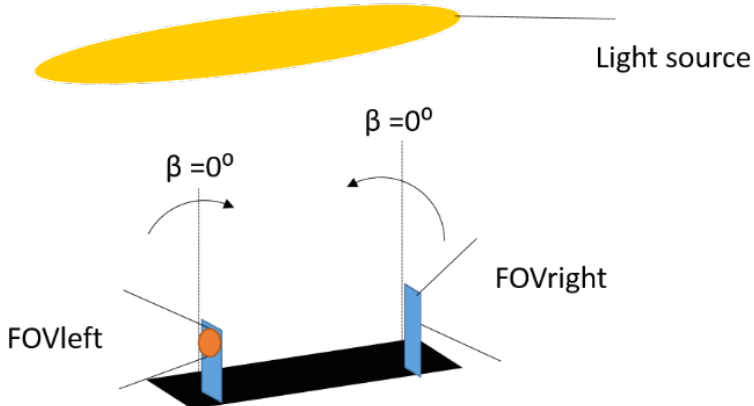


Fig. 41 Bending illustration: The photodiodes should share an intersecting FOV toward the light source for the sensor to operate. Bending values $30^\circ < \beta < 45^\circ$ were observed to give symmetric photodiode outputs. $B = 90^\circ$ completely overlaps the FOVs, without distinct horizons for each photodiode.

3.12 Test Setup Limitations

The maximum motion frequency achieved with the motor is around 10 Hz for velocity mode. For position mode, the frequency is even lower, at 2 Hz. Above these frequencies for related modes, the motor does not follow the input position/velocity. The higher frequency components in the plots are from inherent mechanical vibrations of the motor and the flickering of laboratory lights at 60 Hz or its harmonics at 120–180Hz. The camera used has a theoretical claim of 87 fps frame rate. However, when this frame rate is used, frame drops are observed. Optic flow calculation is highly corrupted by frame drops. Frame drops were minimized with 60 fps frame rate.

Also, using 2 cameras for covering more field was our first attempt. This configuration needs triggering to satisfy that the cameras are taking photo at the same time. Triggering was achieved with 2 PX-4 Inertial Measurement Units working as master and slave. However, data-transfer limitation from USB port reintroduced the lower frame rate problem; hence, frame drops stopped after switching to one camera at the same frame rate. To allow for triggering, frame rate had to be decreased to 20 fps, which limited the optic flow bandwidth. To show the maximum achievable bandwidth for optic flow with this configuration, only one camera is used with 60 fps, 376×240 pixels image.

4. Sensor Fusion

As described in Section 3, ocellar sensor shows a relatively stable magnitude across the test frequencies. Optic flow frequency response can keep up with the ocellar sensor for 60 fps data. As the frame rate decreases, optic flow magnitude plot rolls off. At high motion frequencies (where the optic flow information degrades), it is possible to use the ocellar circuit. This section first presents the biological background for sensor fusion in insect compound eyes and the ocelli. Then the general fusion approaches from the literature are discussed. Finally, the optic flow and the ocellar sensor data are fused to demonstrate the high-frequency roll-off compensation of optic flow, using the ocellar sensor.

4.1 Biological Background for Sensor Fusion

From the behavioral studies, ocelli and compound eyes are thought to work together for flight stabilization abilities.^{21,22,24} In the blowfly, it is previously studied that lobula plate tangential cells estimate the self-motion by taking local motion information from compound eyes. One of the cells that are reported to respond optic flow information is a tangential cell, called V1.⁵⁶ Parsons et al.⁵⁷ reports that V1 responds to ocelli stimulus as well. The response increases with the rate at which the light intensity changes, implying that V1 might be encoding angular velocity information, as well as optic flow information. Haag et al.⁵⁸ experiments that a prominent descending neuron called DNOVS1 receive input from 2 sources—from the photoreceptors of compound eye via large-field motion sensitive cells and from photoreceptors of ocelli via ocellar interneurons. Parsons et al.⁵⁹ reports that lobula plate neurons combine inputs from both ocelli and compound eyes. Ocellar responses encode information in 3 axes, whereas compound eyes encode in 9. This reveals that ocelli are only able to detect rotation around 3 axes, thus offering less specificity with respect to compound eye. If we assume a direct summation of ocelli and compound eye neuronal signals, this might help the flight behavior in 3 axes (since there will be more information for 3 axes, from both compound eyes and ocelli). However, for the other 6 axes, ocelli might output “zero” and the fused response from both compound eye and ocelli might degrade the flight behavior, which seems like counterintuitive. Parsons et al.⁵⁹ suggest that each VS neuron is tuned to the ocellar axis closest to its compound eye axis, combining the speed of ocelli with the accuracy of compound eyes without compromising either.

Having said that ocelli are faster than compound eyes, what is the quantitative difference between these latencies? The response latency depends strongly on experimental parameters, such as contrast and frequency of a moving stimulus. For example, with increasing contrast and high frequency, latency decreases.

Moreover, temperature changes and the age of the fly affect the latency.⁶⁰ Safran et al.⁶¹ report that motion sensitive neuron H1 (compound eye neuron) transmits signals in 20–30 ms. Parsons et al.⁵⁹ measures 6 ms for ocellar latency, which indicates a significant reduction when compared to compound eyes. For high frequency disturbances, low-latency ocellar neurons will be needed.

4.2 Fusion Approaches

In motion detection and control systems, especially in flight control and inertial navigation, different kinds of sensors are used on one platform. When measuring a particular variable, a single type of sensor may not be able to meet all the required performance specifications. For example, both accelerometer and gyroscope data can be used to compute angles. Since an accelerometer gives acceleration, angles can be reconstructed from accelerometer output by 2-fold integration. Similarly, a gyroscope gives velocity information and one integration would be enough. The accelerometer is known to be good for “long term”, meaning that it does not drift. A gyroscope is good for “short term”; it is known to have poor drift characteristics but is able to give a fast response. An ideal combination would be a fast transient response with no drift, by combining good qualities from 2 measurements.

Theoretically, if a time-varying signal is applied to both a low-pass and high-pass filter with unity gain, the sum of the filtered signals should be identical to the input signal. (See Fig. 42.) Assume that x and y are noisy measurements of some signal z , with x employing low-frequency noise and y employing high-frequency noise. z' is the estimate of the signal z produced by the complementary filter.

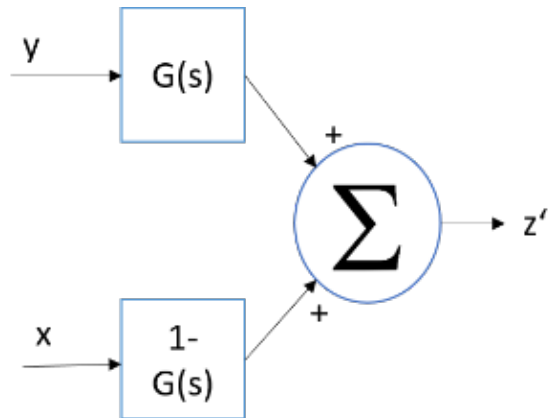


Fig. 42 Illustration of complementary filter

Practically, complementary and Kalman filters provide the fusion of 2 signals. The Kalman filter, working in time domain, needs statistical description of the noise corrupting the signals. This noise is assumed to be Gaussian white noise.

Complementary filters approach the problem from the frequency domain, and they are generally used for the fusion systems that do not deal with noise. For digital implementation, the complementary filter has considerable advantage over the Kalman filter, as Kalman gains are not computed for each state. Therefore, after determining the filter coefficients for complementary filter, the update rate of complementary filter can be higher than Kalman filter for each loop. This is an important consideration for the applications in which high-rate loop closure is necessary.

4.3 Previous Sensor Fusion Implementations

Sensor fusion is governed by complementary and Kalman filtering in the literature, generally for virtual reality applications in computer vision and attitude control. Vision-based information helps avoiding the errors resulting from integrating the inertial sensors over time. Vaganay et al.⁶² fuse 2 accelerometers and 3 gyroscopes for an indoor mobile robot to obtain attitude information using an extended Kalman filter. Foxlin⁶³ fuses gyroscopes and inclinometer for head-tracking using a Kalman filter. You and Neumann⁶⁴ integrate high-frequency stable gyroscope and low-frequency stable vision-based tracking using a Kalman filter for an augmented reality. Wu et al.⁶⁵ use an extended Kalman filter that takes information from camera images, inertial measurement unit, and magnetometers to estimate the pose of the vehicle. Chevron et al.⁶⁶ fuse accelerometer, gyroscope, and vision sensors to obtain position, velocity, and attitude information for an unmanned aerial vehicle (UAV), using a nonlinear complementary filter framework. Bleser and Stricker⁶⁷ use an extended Kalman filter to fuse vision-based output for slow movements and inertial sensor output for fast movements for virtual reality applications. Conte and Doherty⁶⁸ use a Kalman filter to fuse data from 3 accelerometers and 3 gyroscopes with a position sensor for UAV navigation. Position sensor input is either from a global positioning system (GPS), when GPS is available, or from vision system (feature tracking) when GPS is not available. Schall et al.⁶⁹ fuse GPS data, inertial sensor data, and camera image data for global pose information for augmented reality. Inertial and GPS data are fused using a Kalman filter. Achtelik and Weiss⁷⁰ use an extended Kalman filter to fuse air pressure sensor and vision framework (computationally expensive) with inertial sensor data to handle the fast movements and disturbances of the micro-air vehicle. Campolo et al.⁷¹ propose a complementary filter to fuse magnetometer, accelerometer, and gyroscope data for attitude estimation. In this section, the time domain signal of both ocellar and optic flow outputs are combined to extend the optic flow frequency response.

4.4 Ocellar Sensor-Optic Flow Fusion Approach

Previous results show that optic flow shows roll-off at high frequency motion. On the other hand, the ocellar sensor shows a relatively flat response at high frequencies. This experiment uses a camera capable of 87 fps, in theory, and a high-speed Ubuntu laptop. Even with this configuration, the real frame rate obtained from the camera becomes 60 fps because of data transfer limitations of USB busses. The frame rates higher than 60 fps result in dropped frames and corrupt the optic flow output.

Commercially available single-board computers (e.g., Raspberry Pi⁷¹) allow for lower frame rates. Practically, Raspberry Pi 2 is limited to 15–20 fps for the same Lucas–Kanade algorithm used in this experiment. A more expensive model, Odroid XU4,⁷² is capable of 60 fps; however, its cost doubles Raspberry Pi (\$75 vs. \$35). A relatively cheap single-board computer will have a limited optic flow computation bandwidth. On the other hand, the ocellar sensor offers a fast, cheap, and low-power alternative to optic flow computation. It has a relatively flat magnitude and phase response, and it is an attractive alternative for rotational motion. However, its performance is highly dependent on the luminance. It assumes a constant luminance gradient from sky to ground. Optic flow computation does not have such an assumption, and it only needs a texture around it. Moreover, this setup uses a 180°-FOV lens to obtain wide-field motion. To have more FOV, the number of cameras may be increased; this will, however, create the necessity for simultaneous triggering of the 2 cameras. When this setup is used with 2 cameras, the triggering reduces the camera frame rates down to 20 fps. This reduction is expected to be more using a cheaper configuration. Lower frame rate will introduce a lower optic flow bandwidth, making the optic flow sensing incapable of performing at high frequencies. To compensate for the high-frequency roll-off of optic flow, ocellar sensor data are fused with optic flow. Figure 43 shows the complementary fusion. The optic-flow data are low-pass filtered with a fourth-order Butterworth filter. The inverse of this filter, a fourth-order Butterworth high-pass filter, with the same cutoff frequency is used to high-pass filter the ocelli data. The reason for using a fourth-order Butterworth filter instead of single-pole high- and low-pass filters is that it resulted in a better coherence. Single-pole filter combinations decreased the coherence values at high frequencies. The fusion operation increased the bandwidth and decreased the phase delay of optic flow.

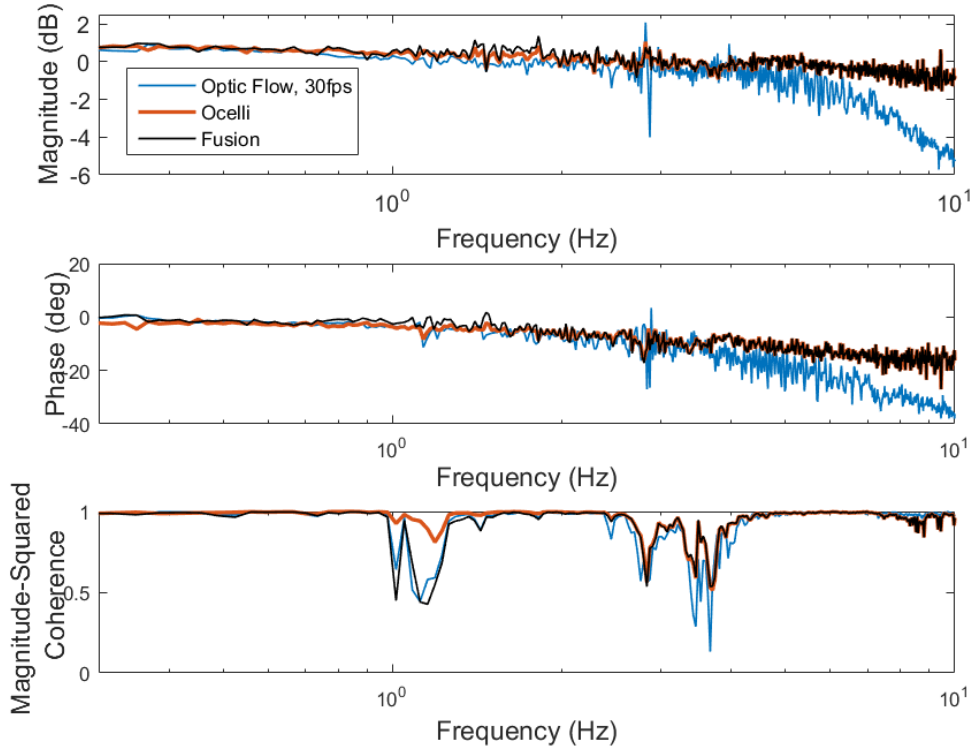


Fig. 43 Frequency response ocelli, optic flow, and their complementary fusion: Fourth-order Butterworth filter was used to high-pass ocelli and low-pass optic flow. The normalized cutoff frequency had to be kept very small to make use of ocelli's relatively flat magnitude and less-delayed phase. Fused response shows coherence is better than optic flows.

An even more direct way is taking the weighted average of optic flow and ocelli. While this approach will not provide fully low-pass filtered optic flow and high-pass filtered ocelli, if the ocelli weight is kept high, the result will be very similar to optic flow. Figure 44 shows another fusion that implements

$$a * \text{ocelli} + (1 - a) * \text{optic flow} \quad (48)$$

where $a = 0.9$. Magnitude, phase, and coherence plots result in-between ocelli and optic flow, very close to ocelli.

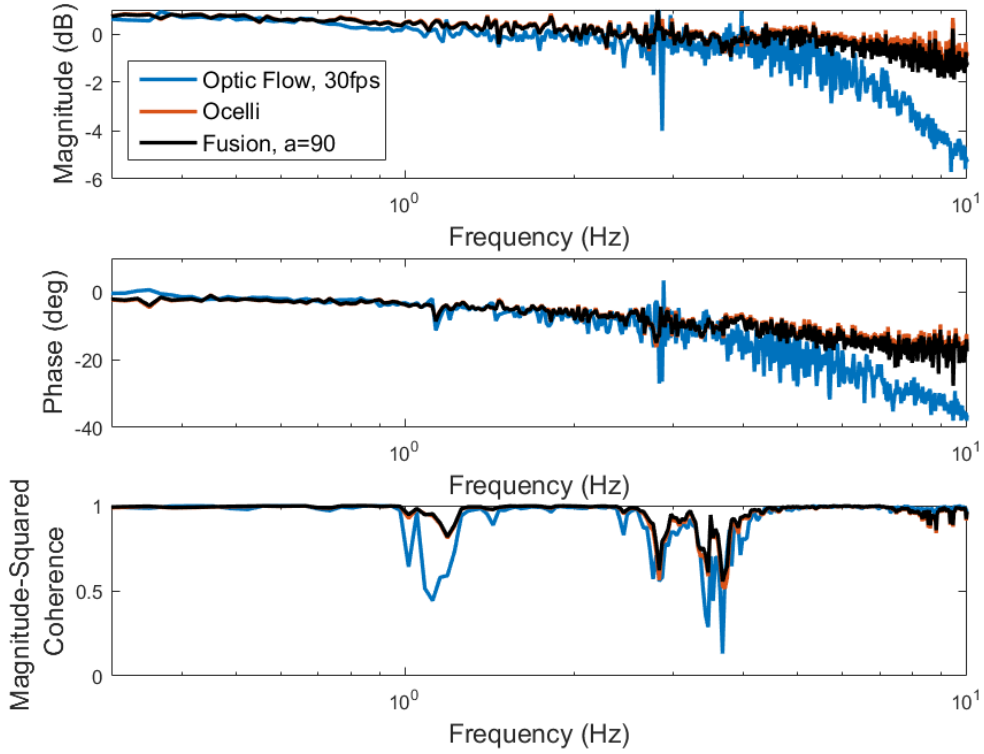


Fig. 44 Frequency response ocelli, optic flow, and their weighted-average fusion: Ocelli and optic flow time-domain signals are combined to obtain a result close to ocelli.

However, complementing both ocelli and optic flow readings gives a result close to ocelli. It assumes that the ambient luminance distribution is as calibrated in this experiment. We know that the ocelli magnitude increases with increasing luminance. This peak-to-peak amplitude is a linear function of input light source power, as seen in Section 3. Additionally, ocellar sensor has to be in a “valid range”. All in all, optic flow is immune to luminance intensity. It gives a flat magnitude response at low frequencies. Ocelli, however, is vulnerable to luminance intensity and it does not show a roll-off in magnitude as optic flow shows. It would be ideal to combine the good properties of both measurements real-time. Ocelli magnitude plot with respect to increasing luminance intensity should result in a plot like Fig. 45. Optic flow magnitude plot shows low-pass characteristics.

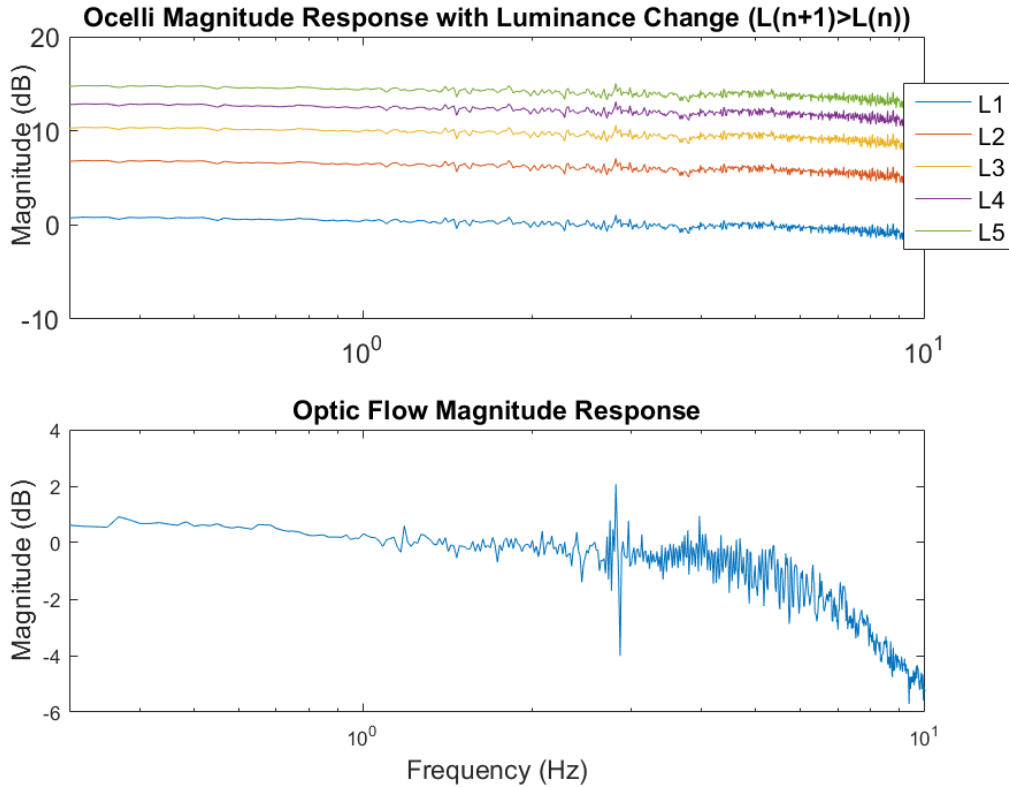


Fig. 45 Magnitude response of ocelli with different luminance values and optic flow at 30 fps: Increasing luminance implies higher magnitude for ocelli ($L_1 < L_2 < L_3 < L_4 < L_5$). Ambient luminance change brings adaptive gain necessity. Upper figure is the magnitude-scaled versions of ocelli response, not derived from real luminance values.

A mechanism that allows for switching from one mode to another is desired to decide which sensor to use. This switching mechanism may be a gyroscope. The gain adjustment may be done with a feedback from ocelli output that is continuously compared with gyroscope/optic flow output. If a valid region for ocelli is found, ocelli is preferred over optic flow due to its high speed. A hypothetical iterative approach is shown in Fig. 46. First, ocelli gain is adjusted with the use of a lookup table and the error between ocelli and gyro is computed. If this error is below a threshold, the gain adjustment is satisfied. After this, the validity of ocelli output is confirmed by computing the error between the gyro and optic flow. If these comparisons allow, ocelli is preferred to be used for closed-loop rate stabilization. If not, either gyro or optic flow is used. Ocelli gain can be adjusted with digital potentiometers and an operational amplifier. The digital potentiometers are controlled from microcontroller. For a gain less than 1, a voltage divider reduces the ocelli output. For a gain greater than 1, a noninverting amplifier increases the ocelli output. This output is continuously fed back to the microcontroller to compare the gyroscope and ocelli error to find a new gain value from the lookup

table and adjust the potentiometers accordingly. Figure 47 shows the possible circuit configuration with microcontroller.

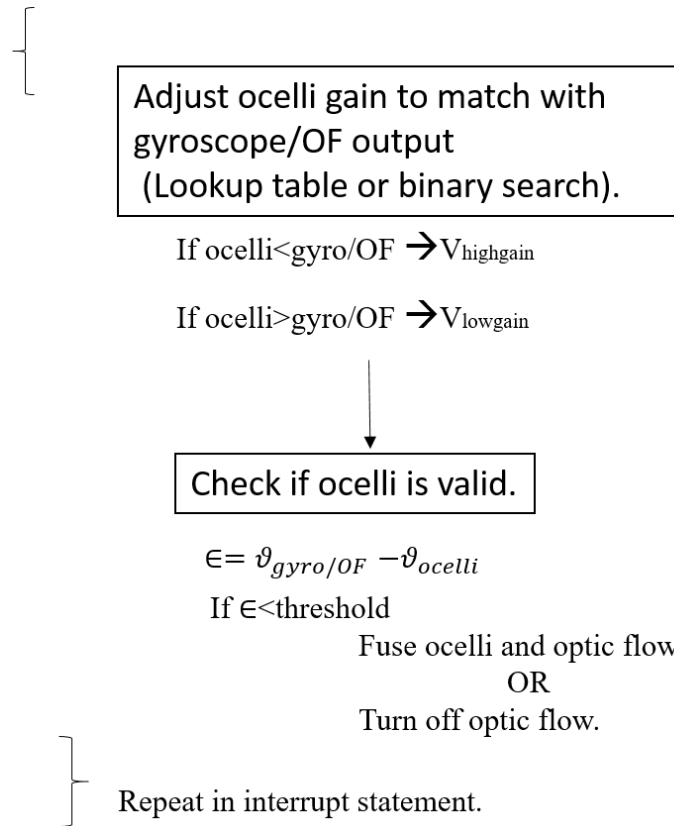


Fig. 46 Hypothetical sensor decision approach: Adjust ocelli gain by continuously computing error between gyro/OF and ocelli; check if ocelli is valid to use by comparing gyro/OF; use ocelli if comparisons allow.

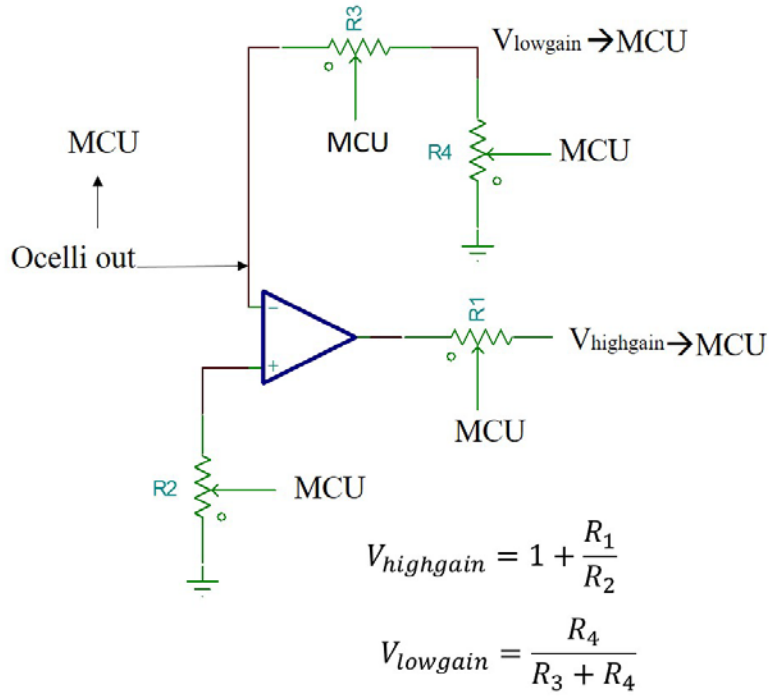


Fig. 47 Hypothetical ocelli gain adjustment approach: Gains > 1 are tuned by noninverting op-amp. Gains < 1 are tuned by voltage divider. The tuned outputs are compared with lookup table and microcontrollers iteratively tune the digital potentiometers until error threshold is low enough.

5. Conclusion and Future Work

5.1 Conclusion

Frequency-domain characterization of optic flow and ocellar sensors are presented. The advantages and disadvantages for both sensing mechanisms are discussed. In summary:

- Ocellar sensor shows a relatively flat magnitude response and less phase delay than optic flow.
- Ocellar sensor is attractive for high-rate loop closure since it is cheaper and faster than high-quality cameras.
- The displacement dynamic range of the ocellar sensor is observed to be 1 radian with this setup, due to the small size of the light source. Using a larger light source, higher displacements may be achieved.
- The frequency dynamic range of ocellar sensor is observed to be up to 10 Hz with motion and up to low-frequency cutoff without motion. Ten

hertz is a limitation from mechanical test setup; higher motion frequencies are expected due to the circuit simulation and LED experiment results. For outdoor experiments, the low-frequency cutoff of the band-pass circuit can be eliminated since there is no flickering issue outdoors.

- Ocellar sensor magnitude shows a linear relationship with luminance intensity. Since it is highly luminance-dependent, an adaptive gain calibration is necessary for usage with different luminance levels.
- Ocellar sensor shows monotonic increase with increasing gyro values.
- Optic flow magnitude rolls off at high frequencies. Specifically, 60 fps can keep up with ocelli response. Thirty and 20 fps show roll-off at 7 Hz. Less frame rate shows steeper roll-off. Phase delay increases with increasing frequency. All frame rates tested show the same phase delay across all frequencies.
- Optic flow algorithm parameters (feature points, window size) affect the coherence. No significant change in magnitude and phase plots is observed, except for erroneous magnitudes for extremely small window sizes or feature points.

5.2 Future Work

Several potential directions may be taken to extend the work of this report. Taking the characterization results, performance parameters, and hypothetical sensor fusion suggestions into account, a closed-loop optic flow and ocellar-based fusion may be implemented to perform real-time stabilization and disturbance rejection. Multiple ocellar sensors with lenses may be placed in an array-like fashion on a flying vehicle to extend the current FOV of the ocellar sensor. The outputs of ocellar sensor may be matched with predefined patterns to inform where exactly the disturbance occurs.

The combination of optic flow computations and ocellar sensor gives both slow and fast alternatives for horizon detection and angular-rate sensing.

The coherence in ocellar sensor and optic flow frequency response plots show dips at specific frequencies. The reason for these dips could not be identified during the experiments. If these dips were caused from the motor mechanical noise, both the gyroscope and the ocellar sensor should be able to pick the mechanical noise up, resulting in the same motion for both of them. Also, the motor resonance and gyroscope resonance possibilities have been eliminated after confirming the time-domain signals with the ground truth. It is presumed that the ocellar sensor may be

slightly modulating the input sine wave at these frequencies. The experiments can be repeated by using another ocellar sensor board and/or another motor.

To compensate for the optic flow's slow rate, another direction might be converting the optic flow-ocelli system to a fully analog scheme. Combining both sensors in analog domain might give the complementary approach in a compact, fast, and lightweight way. While digital optic flow computation has the freedom of easy adaptation and reconfiguration with different, sophisticated, and robust algorithms, subthreshold analog very-large-scale integration (VLSI) optic flow designs are much smaller, lightweight, low power, and faster. One may argue that the one-board computers are already lightweight. However, decrease in size and weight are extremely important factors for micro aerial vehicle design. VLSI allows the photodiodes and computation circuitry to be fabricated on a piece of silicon; therefore, it is very suitable for vision-based sensing.

Insect ocelli have high responsivity to ultraviolet wavelengths. A completely different direction might be taking the ocellar sensor outside, using the sky-ground discrimination in ultraviolet wavelengths. The wideband photodiodes in current circuit can be replaced with ultraviolet photodiodes. A detail to consider is the ultraviolet intensity difference in sky and ground in different times of the day and different weather conditions. On a sunny day, the results show that sky is brighter than ground in ultraviolet. On a cloudy day, it can be the opposite. While the constant and negative luminance gradient may not be satisfied for all cases, specific weather conditions (e.g., sunny day, no clouds) can allow for outdoor use. We have built the ultraviolet version of the ocellar sensor and tested outside. A main problem is the uneven ultraviolet intensity coming to both ultraviolet photodiodes. On cloudy days, there is nearly no ultraviolet difference between sky and the ground; it is thought that the clouds are blocking the ultraviolet portion in the sunlight. On sunny days, one photodiode should not see the high intensity created by the sun and should only have the portion coming from the sky. The instantaneous displacement of the clouds and the wind are also factors that create the uneven ultraviolet intensity on both photodiodes. While these cases make it hard to test outside, we have seen with some datasets that it agrees with gyroscope output.

6. References

1. Barth FG, Humphrey J, Srinivasan M. *Frontiers in sensing: from biology to engineering*. Wien (Austria): Springer Business & Media; 2012 [accessed 2016 May 6]. p. 4. E-book URL: <http://www.springer.com/us/book/9783211997482>.
2. Mazokhin GA. *Insect vision*. New York (NY): Plenum Press; 1969.
3. Horridge GA. *Compound eye and vision of insects*. New York (NY): Oxford University Press; 1975.
4. Heisenberg M, Reinhard W. *Vision in Drosophila: genetics of microbehavior*. Berlin (Germany): Springer-Verlag; 1984. pp.82–94
5. Parsons M, Krapp HG, Laughlin SB. Sensor fusion in identified visual interneurons. *Current Biology*. 2010;20(7): London, UK.
6. Safran MN, Flanagan V, Borst A, Sompolinsky H. Adaptation and information transmission in fly motion detection. *Journal of Neurophysiology*. 2007;98(6): Jerusalem, Israel.
7. Joesch M, Schnell B, Shamprasad VR, Reiff DF, Borst A. On and off pathways in *Drosophila* motion vision. *Nature*. 2010;468(7321): Martinsried, Germany.
8. Borst A. Fly visual course control: behavior, algorithms and circuits. *Nature Reviews Neuroscience*. 2014;15(9): Martinsried, Germany.
9. Wallace GK. Visual scanning in the desert locust *Schistocerca gregaria* Forskal. *Journal of Experimental Biology*. 1959;36(3): Reading, UK.
10. Silies M, Gohl D, Clandinin TR. Motion-detecting circuits in flies: Coming into view. *Annual Review of Neuroscience*. 2014;37(307–27): Stanford, CA.
11. Kral K, Michael P. Motion parallax as a source of distance information in locusts and mantids. *Journal of Insect Behavior*. 1997;10(1): Graz, Austria.
12. Sobel EC. The locust's use of motion parallax to measure distance. *Journal of Comparative Physiology A*. 1990;167(5): Philadelphia, PA.
13. Schnell B, Joesch M, Forstner F, Raghu SV, Otsuna H, Ito K, Borst A, Reiff DF. Processing of horizontal optic flow in three visual interneurons of the *Drosophila* brain. *Journal of Neurophysiology*. 2010;103(3): Martinsried, Germany.

14. Haag J, Denk W, Borst A. Fly motion vision is based on Reichardt detectors regardless of the signal-to-noise ratio. *Proceedings of the National Academy of Sciences of the United States of America*. 2004;101(46): Heidelberg, Germany.
15. Frye M. Elementary motion detectors. *Current Biology*. 2015;25(6): Los Angeles, CA.
16. Ocellus cross section. San Francisco (CA): Wikimedia; 2011 [accessed 2016 May 6].
https://commons.wikimedia.org/wiki/File:Insect_ocellus_diagram.svg
17. Stange G, Stowe S, Chahl JS, Massaro A. Anisotropic imaging in the dragonfly median ocellus: a matched filter for horizon detection. *Journal of Comparative Physiology*. 2002;A188(6): Canberra, Australia.
18. Wilson M. The functional organisation of locust ocelli. *Journal of comparative physiology*. 1978;124(4): Canberra, Australia.
19. Goodman LJ. Organisation and physiology of the insect dorsal ocellar system. *Handbook of Sensory Physiology*. New York (NY): Springer; 1981.
20. Kastberger G, Schumann K. Ocellar occlusion effect on the flight behavior of homing honeybees. *Journal of Insect Physiology*. 1993;39(7): Graz, Austria.
21. Schricker B. Die Orientierung der Honigbiene in der Dämmerung. *Zeitschrift für vergleichende Physiologie*. 1965;49(5): Munich, Germany. Summary in English [accessed 2016 May 6]:
<http://link.springer.com/article/10.1007/BF00298112#Abs2>
22. Stange G, Howard J. An ocellar dorsal light response in a dragonfly. *Journal of Experimental Biology*. 1979;83: Canberra, Australia.
23. Stange G. The ocellar component of flight equilibrium control in dragonflies. *Journal of Comparative Physiology*. 1981;141(3): Canberra, Australia.
24. Taylor CP. Contribution of compound eyes and ocelli to steering of locusts in flight: I. Behavioural analysis. *Journal of Experimental Biology*. 1981;93(1): Berkeley, CA.
25. Schuppe H, Hengstenberg R. Optical properties of the ocelli of Calliphora erythrocephala and their role in the dorsal light response. *Journal of Comparative Physiology A*. 1993;173(2): Tubingen, Germany.

26. Rence BG, Lisy MT, Garves BR, Quinlan BJ. The role of ocelli in circadian singing rhythms of crickets. *Physiological Entomology*. 1988;13(2): Appleton, WI.
27. Sprint MM, Eaton JL. Flight behavior of normal and anocellate cabbage loopers. *Annals of the Entomological Society of America*. 1987;80(4): Virginia, VA.
28. Eaton JL, Tignor KR, Holtzman GI. Role of moth ocelli in timing flight initiation at dusk. *Physiological Entomology*. 1983;8(4): Virginia, VA.
29. Wunderer H, Jacobus JDK. Dorsal ocelli and light-induced diurnal activity patterns in the arctiid moth *Creatonotos transiens*. *Journal of Insect Physiology*. 1989; 35(2): Regensburg, Germany.
30. Land MF, Nilsson DE. Animal eyes. 2nd ed. New York (NY): Oxford University Press; 2002.
31. Kirschfeld K. The resolution of lens and compound eyes. In: Neural principles in Vision. Berlin (Germany): Springer; 1976. p. 354–370.
32. Krapp HG, Hengstenberg R. Estimation of self-motion by optic flow processing in single visual interneurons. *Nature*. 1996;384(6608): Tubingen, Germany.
33. Barrows GL, Chahl JS, Srinivasan MV. Biomimetic visual sensing and flight control. *Proceedings of Bristol UAV Conference*, 2002; Bristol, UK.
34. Neumann TR, Bülthoff HH. Insect inspired visual control of translatory flight. *The 6th European Conference on Artificial Life*; 2001; Czech Republic.
35. Neumann TR, Bülthoff HH. Behavior-oriented vision for biomimetic flight control. *Proceedings of the EPSRC/BBSRC International Workshop on Biologically Inspired Robotics*; 2002; Bristol, UK.
36. Wu WC, Schenato L, Wood RJ, Fearing RS. Biomimetic sensor suite for flight control of a micromechanical flying insect: design and experimental results. *IEEE International Conference on Robotics and Automation*; 2003; Taipei, Taiwan.
37. Schenato L, Wu WC, Sastry S. Attitude control for a micromechanical flying insect via sensor output feedback. *IEEE Transactions on Robotics and Automation*. 2004;20(1): Berkeley, CA.

38. Javaan C, Thakoor S, Le Bouffant N, Stange G, Srinivasan MV, Hine B, Zornetzer S. Bioinspired engineering of exploration systems: a horizon sensor/attitude reference system based on the dragonfly ocelli for mars exploration applications. *Journal of Robotic Systems*. 2003;20(1): Canberra, Australia.
39. Kerhuel L, Viollet S, Franceschini N. Steering by gazing: An efficient biomimetic control strategy for visually guided micro aerial vehicles. *IEEE Transactions on Robotics*. 2010;26(2): Paris, France.
40. Moore RJD, Thurrowgood S, Bland D. A fast and adaptive method for estimating UAV attitude from the visual horizon. *IEEE/RSJ International Conference on Intelligent Robots and Systems*; 2011; San Francisco, CA.
41. Javaan C, Akiko M. Biomimetic attitude and orientation sensors. *IEEE Sensors Journal*. 2012;12(2): Edinburgh, Australia.
42. Gremillion G, Humbert JS, Krapp HG. Bio-inspired modeling and implementation of the ocelli visual system of flying insects. *Biological Cybernetics*. 2014;108(6): College Park, MD.
43. Menzel R. Spectral sensitivity and color vision in invertebrates. In: *Comparative physiology and evolution of vision in invertebrates*. Berlin (Germany): Springer Berlin Heidelberg; 1979. p. 503–580.
44. Fahle M, Poggio T. Visual hyperacuity: spatiotemporal interpolation in human vision. *Proceedings of the Royal Society of London B: Biological Sciences*. 1981;213(1193): Tubingen, Germany.
45. Adelson EH, Bergen JR. Spatiotemporal energy models for the perception of motion. *The Journal of the Optical Society of America*. 1985;72(2): Princeton, NJ.
46. Herault J. Vision: Images, Signals and Neural Networks, *Progress in Neural Processing*. Singapore: World Scientific, 2010. p.126.
47. Barron JL, Thacker NA. Tutorial: Computing 2D and 3D optical flow. Manchester (UK): University of Manchester; 2005 [accessed 2016 May 6]. <http://tina.wiau.man.ac.uk/docs/memos/2004-012.pdf>.
48. Lucas BD, Kanade T. An iterative image registration technique with an application to stereo vision. *Proceedings on the 7th International Conference on Artificial Intelligence*; 1981; Vancouver, Canada. p. 674–679.
49. Horn BK, Schunck BG. Determining optical flow. *Technical Symposium East*. International Society for Optics and Photonics, 1981.

50. Stanford mobile computer vision lecture. Stanford (CA): Stanford University; 2015 Apr 20 [accessed 2016 May 6].
<http://web.stanford.edu/class/cs231m/lectures/lecture-7-optical-flow.pdf>.
51. Bouguet JY. Pyramidal implementation of the affine Lucas-Kanade feature tracker description of the algorithm. Santa Clara (CA): Intel Corporation; 2001 [accessed 2016 May 6].
http://robots.stanford.edu/cs223b04/algo_affine_tracking.pdf.
52. Farnebäck G. Two-frame motion estimation based on polynomial expansion. Scandinavian Conference on Image Analysis; 2003; Halmstad, Sweden; p. 363–370.
53. Smartmotor developer's guide. Mountainview (CA): Moog Animatics, [accessed 2016 May 6]. <http://www.animatics.com/support/download-center.html>.
54. Hori M, Shibuya K, Sato M, Saito Y. Lethal effects of short-wavelength visible light on insects. *Scientific Reports*. 2014;4(7383): Sendai, Japan.
55. Scheider K, Conroy J, Nothwag W. Computing optic flow with ArduEye vision sensor. Adelphi (MD): Army Research Laboratory (US); 2013 Jan. Report No.: ARL-TR-6292.
56. Krapp HG, Hengstenberg R., Egelhaaf, M. Binocular contributions to optic flow processing in the fly visual system. *Journal of Neurophysiology*. 2001;85(2): Beilefeld, Germany.
57. Parsons M, Krapp HG, Laughlin SB. A motion-sensitive neuron responds to signals from the two visual systems of the blowfly, the compound eyes and ocelli. *Journal of Experimental Biology*. 2006;209(22): Cambridge, UK.
58. Haag J, Wertz A, Borst A. Integration of lobula plate output signals by DNOVS1, an identified premotor descending neuron. *The Journal of Neuroscience*. 2007;27.8: Martinsried, Germany.
59. Parsons M, Krapp HG, Laughlin SB. Sensor fusion in identified visual interneurons. *Current Biology*. 2010;20(7): London, UK.
60. Warzecha AK, Egelhaaf, M. Response latency of a motion-sensitive neuron in the fly visual system: dependence on stimulus parameters and physiological conditions. *Vision Research*. 2000;40(21): Beilefeld, Germany.
61. Safran MN, Flanagan V, Borst A, Sompolsky H. Adaptation and information transmission in fly motion detection. *Journal of Neurophysiology*. 2007;98(6): Jerusalem, Israel.

62. Vaganay J, Aldon MJ, Fournier A. Mobile robot attitude estimation by fusion of inertial data. IEEE International Conference on Robotics and Automation; 1993; Atlanta, GA.
63. Foxlin E. Inertial head-tracker sensor fusion by a complementary separate-bias Kalman filter. Proceedings of the IEEE Virtual Reality Annual International Symposium; 1996.
64. You S, Neumann U. Fusion of vision and gyro tracking for robust augmented reality registration. Proceedings of IEEE Virtual Reality; 2001.
65. Wu AD, Johnson EN, Proctor AA. Vision-aided inertial navigation for flight control. Journal of Aerospace Computing, Information, and Communication. 2005;2.9: Atlanta, GA.
66. Cheviron T, Hamel T, Mahony R, Baldwin G. Robust nonlinear fusion of inertial and visual data for position, velocity and attitude estimation of UAV. IEEE International Conference on Robotics and Automation; 2007.
67. Bleser G, Stricker D. Advanced tracking through efficient image processing and visual-inertial sensor fusion. IEEE Visual Reality; 2008; Reno, NV.
68. Conte, G, Doherty P. Vision-based unmanned aerial vehicle navigation using geo-referenced information. EURASIP Journal on Advances in Signal Processing. 2009;2009(387308): Linkopig, Sweden.
69. Schall G, Wagner D, Reitmayer G, Taichmann E, Wieser M, Schmalstieg D, Hofmann-Wellenhof B. Global pose estimation using multi-sensor fusion for outdoor augmented reality. 8th IEEE International Symposium on Mixed and Augmented Reality; 2009.
70. Achtelik M, Weiss S. Onboard IMU and monocular vision based control for MAVs in unknown in-and outdoor environments. IEEE International Conference on Robotics and Automation; 2011.
71. Campolo D, Schenato L, Pi L, Deng X, Guglielmelli E. Attitude estimation of a biologically inspired robotic housefly via multimodal sensor fusion. Advanced Robotics. 2009;23(2009): Rome, Italy.
72. Raspberry Pi model summaries. San Francisco (CA): Wikipedia [accessed 2016 May 6]. https://en.wikipedia.org/wiki/Raspberry_Pi.
73. Odroid XU4 summary. GyeongGi (South Korea): Odroid [accessed 2016 May 6]. http://www.hardkernel.com/main/products/prdt_info.php?g_code=G143452239825.

List of Symbols, Abbreviations, and Acronyms

2-D	2-dimensional
AC	alternating current
ADC	analog-to-digital converter
DC	direct current
EMD	elementary motion detector
FOV	field of view
fps	frames per second
GPS	global positioning system
LED	light-emitting diode
LSB	least significant bytes
MCU	Microcontroller Unit
MSB	most significant bytes
SPI	serial peripheral interface
sUAS	small unmanned aircraft systems
UAV	unmanned aerial vehicle
VLSI	very-large-scale integration

1 DEFENSE TECHNICAL
(PDF) INFORMATION CTR
DTIC OCA

2 DIRECTOR
(PDF) US ARMY RESEARCH LAB
RDRL CIO L
IMAL HRA MAIL & RECORDS
MGMT

1 GOVT PRINTG OFC
(PDF) A MALHOTRA

1 US ARMY RESEARCH LAB
(PDF) RDRL SER L
JOSEPH K CONROY

1 UNIV OF MD OR GA TECH
(PDF) NIL GUREL

1 UNIV OF MD
(PDF) TIMOTHY HORIUCHI

1 UNIV OF COLORADO
(PDF) SEAN HUMBERT